COMPUTATIONAL MODELING AND EXPERIMENTAL VALIDATION OF THE PHOTOTHERMAL ACTIVITY OF METAL ION-CHELATED NATURAL MELANIN NANOPARTICLES

by

Şeyma Yektar

B.S., in Biomedical Engineering, Yıldız Technical University, 2022

Submitted to the Institute of Biomedical Engineering
in partial fulfillment of the requirements
for the degree of
Master of Science
in
Biomedical Engineering

Boğaziçi University
2025

COMPUTATIONAL MODELING AND EXPERIMENTAL VALIDATION OF THE PHOTOTHERMAL ACTIVITY OF METAL ION-CHELATED NATURAL MELANIN NANOPARTICLES

APPROVED BY:

Assist. Prof. Dr. Mustafa Kemal Ruhi .....
(Thesis Advisor)

Assist. Prof. Dr. Engin Baysoy .....
(Thesis Co-advisor)

Assist. Prof. Dr. Pınar S. Özbay .....

Assist. Prof. Dr. Canan Kurşungöz Bağcı .....

Assist. Prof. Dr. Gizem Kaleli Can .....

DATE OF APPROVAL:

ACKNOWLEDGMENTS

I would like to express my deepest gratitude to my advisor, Asst. Prof. Dr. Mustafa Kemal Ruhi, and my co-advisor, Asst. Prof. Dr. Engin Baysoy, for their invaluable support, guidance, and encouragement throughout the course of my thesis. Their profound knowledge, insightful feedback, and unwavering patience have been instrumental in the successful completion of this study.

It has also been a privilege to share this journey with my lab mates and colleagues, whose experience, suggestions, and camaraderie have greatly enriched both the research process and the personal experience of working in an academic environment. Their presence has turned this challenging process into a collaborative and fulfilling one.

My heartfelt thanks go to my dear friend and colleague, Süeda Kaya, for her unwavering encouragement, assistance, and friendship. Her continuous support has been a source of motivation and strength, and I am truly grateful to have had her by my side throughout this journey.

Above all, I would like to extend my deepest appreciation to my beloved parents. Their endless love, sacrifices, and steadfast belief in me have been the foundation of all my achievements. They have stood by me through every challenge and triumph with unyielding support and devotion. I am forever grateful and love them dearly. Your faith in me has made all of this possible.

This study was supported by Boğaziçi University Research Fund Grant Number 20333.

ACADEMIC ETHICS AND INTEGRITY STATEMENT

I, Şeyma Yektar, hereby certify that I am aware of the Academic Ethics and Integrity Policy issued by the Council of Higher Education (YÖK) and I fully acknowledge all the consequences due to its violation by plagiarism or any other way.

Name :

Signature:

Date:

ABSTRACT

COMPUTATIONAL MODELING AND EXPERIMENTAL VALIDATION OF THE PHOTOTHERMAL ACTIVITY OF METAL ION-CHELATED NATURAL MELANIN NANOPARTICLES

Melanin, a naturally occurring biopolymer, serves as a pigment and protective agent in organisms such as animals, fungi, and bacteria. Melanin nanoparticles, which can be obtained naturally or synthetically, are frequently investigated in many biomedical applications due to their high biocompatibility, biodegradability, antioxidant properties, and visible light absorption properties. In addition, the chemical structures of melanin nanoparticles allow them to chelate drugs, various biomolecules, and metal ions such as Fe^{3+}, Cu^{2+}, Gd^{3+}, Mn^{2+}. It has been shown that melanin nanoparticles chelated to metal ions can also be used as a contrast agent by shortening the T1 relaxation time in magnetic resonance imaging. With these properties, melanin nanoparticles are being investigated for both imaging and treatment, i.e. theranostic purposes. However, the effect of nanoparticle size and the wavelength of the applied light on PTT efficiency, as well as the impact of metal ion chelation of melanin nanoparticles on photothermal performance, has not been comprehensively investigated in the literature, to the best of our knowledge. This study aims to investigate these effects through modeling and in vitro experiments. Answering these questions will enable the determination of the most appropriate nanoparticle size and irradiation parameters, and will pave the way for temperature-controlled PTT applications and optimization of treatment efficiency.

Keywords: Photothermal Therapy, Melanin Nanoparticles, Theranostic Applications

ÖZET

METAL İYON ŞELATLI DOĞAL MELANİN NANOPARÇACIKLARIN FOTOTERMAL AKTİVİTESİNİN HESAPLAMALI MODELLEMESİ VE DENEYSEL DOĞRULANMASI

Doğal olarak oluşan bir biyopolimer olan melanin; hayvanlar, mantarlar ve bakteriler gibi organizmalarda pigment ve koruyucu madde olarak görev yapmaktadır. Doğal veya sentetik yollarla elde edilebilen melanin nanoparçacıklar; yüksek biyouyumlulukları, biyobozunur olmaları, antioksidan özellikleri ve görünür ışığı soğurma özellikleri nedeniyle birçok biyomedikal uygulamada sıklıkla araştırılmaktadır. Ayrıca melanin nanoparçacıkların kimyasal yapıları ilaç, çeşitli biyomolekül ve Fe^{3+}, Cu^{2+}, Gd^{3+}, Mn^{2+} gibi metal iyonlarını şelatlamaya olanak sağlar. Metal iyonlarına şelatlanmış melanin nanoparçacıkların, manyetik rezonans görüntülemede T1 gevşeme süresi kısaltıcı etki yaratarak kontrast ajanı olarak da kullanılabildiği gösterilmiştir. Melanin nanoparçacıklar bu özellikleri ile aynı anda hem görüntüleme hem de tedavi, yani teranostik amaçlı araştırılmaktadır. Ancak nanoparçacık boyutunun ve uygulanan ışığın dalga boyunun FTT etkinliği üzerindeki etkisi ile melanin nanoparçacıklarının metal iyonlarıyla şelatlanmasının fototermal performansa katkısı, mevcut literatür bilgisine göre daha önce kapsamlı bir şekilde araştırılmamıştır. Bu çalışma modelleme ve in vitro deneyler yoluyla bu etkilerin araştırılmasını amaçlamaktadır. Bu soruların cevaplanması melanin nanoparçacıklar ile yapılan uygulamalardaki en uygun nanoparçacık boyutu ve ışınlama parametrelerinin belirlenmesini sağlayacak ve sıcaklık kontrollü FTT uygulamalarının optimize edilmesinin yolu açılmış olacaktır.

Anahtar Sözcükler: Fototermal Terapi, Melanin Nanoparçacıklar, Teranostik Uygulamalar

TABLE OF CONTENTS

ACKNOWLEDGMENTS iii
ACADEMIC ETHICS AND INTEGRITY STATEMENT iv
ABSTRACT v
ÖZET vi
LIST OF FIGURES ix
LIST OF TABLES xi
LIST OF SYMBOLS xii
LIST OF ABBREVIATIONS xiv
1. INTRODUCTION 1
1.1 Motivation and Objectives 1
1.2 Organization of Thesis 3
2. BACKGROUND 4
2.1 Conventional and Alternative Treatment Methods for Cancer 4
2.2 Photothermal Therapy (PTT) 5
2.3 Melanin Nanoparticles (MNPs) 6
3. MATERIALS AND METHODS 12
3.1 Synthesis of Nanoparticles 12
3.2 Characterization of Nanoparticles 13
3.3 Simulation of the Effect of Melanin Nanoparticle Sizes and Light Used in PTT on Temperature Increase 15
3.3.1 Design and Geometry 17
3.3.2 Definition and Calculation of Material and Electrical Properties 19
3.3.3 Definition of Boundary Conditions 21
3.3.4 Definition of Mesh Structure 22
3.3.5 Thermal Analysis and Energy Transfer 22
3.4 Simulation of How MNPs Chelated with Fe^{3+} Ions Effect PTT Efficiency 24
3.4.1 Design and Geometry 24
3.4.2 Definition and Calculation of Material and Electrical Properties 25
3.4.3 Electromagnetic Wave Simulation 25

3.4.4 Heat Transfer Coupling 26
3.4.5 Study Sequence and Result Evaluation 27
3.5 Excitation of MNPs with 530 nm, 633 nm and 785 nm Light Sources and Comparison of Results with Thermocouple 28
4. RESULTS 30
4.1 Synthesis and Characterization of MNPs 30
4.1.1 Size and Distribution Analysis by DLS 30
4.1.2 Functional Group Analysis by FTIR 33
4.1.3 Optical Properties by UV-Vis Spectroscopy 34
4.1.4 Morphological Characterization by SEM 35
4.2 Simulation Results 38
4.2.1 Heat Distribution Profiles in Simulations 38
4.2.2 Surface Temperature Profiles 41
4.2.3 Electric Field Profile 45
4.3 Experimental Results 47
4.3.1 Photothermal Heating Under Light Source Irradiation 47
4.4 Comparison of Simulation and Experimental Results 49
4.5 Summary of Key Findings 50
5. DISCUSSION 52
6. CONCLUSION 61
REFERENCES 62

LIST OF FIGURES

Figure 3.1	Synthesis of MNPs and MNP-Fe^{3+}s from cuttlefish ink.	12
Figure 3.2	Simulation workflow.	15
Figure 3.3	Geometry of the MNP.	18
Figure 3.4	Ellipsometric characterization of melanin. Refractive index n (black) and extinction coefficient k (red) determined via variable angle spectroscopic ellipsometry [45].	19
Figure 3.5	PML surrounding a nanosphere for domain truncation in calculations.	22
Figure 4.1	Size-intensity distribution comparison of MNPs and MNP-Fe^{3+}s.	31
Figure 4.2	Size-intensity distribution comparison of MNPs and MNP-Fe^{3+}s.	32
Figure 4.3	FTIR spectra of MNPs and MNP-Fe^{3+}s.	34
Figure 4.4	UV-Vis absorption comparison of MNP and MNP-Fe^{3+}s.	34
Figure 4.5	SEM images of MNPs.	36
Figure 4.6	SEM images of MNP-Fe^{3+}s.	37
Figure 4.7	Heat distribution profile of MNP dispersed in water after simulation of 530 nm light source irridation.	39
Figure 4.8	Heat distribution profile of MNP-Fe^{3+} dispersed in water after simulation of 530 nm light source irridation.	40
Figure 4.9	The surface temperature distribution obtained from the simulation for MNP under 530 nm laser irradiation in distilled water.	42
Figure 4.10	The isothermal surface temperature distribution obtained from the simulation for MNP under 530 nm laser irradiation in distilled water.	43
Figure 4.11	The surface temperature distribution obtained from the simulation for MNP under 530 nm laser irradiation in blood.	44
Figure 4.12	Electric field distribution of MNP under light source irradiation.	45
Figure 4.13	Absorption cross-section spectra of MNP with different radii.	46
Figure 4.14	Absorption cross-section spectra of MNP-Fe^{3+} with different radii.	46

Figure 4.15 Comparison of the temperatures obtained with the 530 nm light source. 48
Figure 4.16 Comparison of the temperatures obtained with the 633 nm light source. 48
Figure 4.17 Comparison of the temperatures obtained with the 785 nm light source. 49
Figure 4.18 Comparison of simulation and experimental results. 49
Figure 4.19 Correlation plot comparing the simulated and experimental temperature values. 50

LIST OF TABLES

Table 3.1	Refractive index n and extinction coefficient k of MNP for the specified wavelengths.	20
Table 3.2	Physical properties of MNP dispersions in various media.	23
Table 3.3	Physical properties of MNP-Fe^{3+} dispersions in various media.	26
Table 4.1	DLS measurements of MNPs and MNP-Fe^{3+}s.	32
Table 4.2	Comparison of FTIR spectral bands of MNPs and MNP-Fe^{3+}s.	33
Table 4.3	Absorbance characteristics of MNPs and MNP-Fe^{3+}s.	35
Table 4.4	Comparison of temperature changes after light source irridation simulations of MNP and MNP-Fe^{3+}.	40
Table 4.5	Comparison of simulated temperature changes of MNP with different sizes after light source irradiation.	41
Table 4.6	Comparison of simulated temperature changes of MNP-Fe^{3+} with different sizes after light source irradiation.	41
Table 4.7	Highest temperatures recorded after light source irridation MNPs and MNP-Fe^{3+}s.	47

LIST OF SYMBOLS

Fe^{3+}	Iron
Mn^{2+}	Manganese
Gd^{3+}	Gadolinium
Cu^{2+}	Copper
nm	Nanometer
mL	Milliliter
mg/mL	Milligram per Milliliter
mW	Milliwatts
mW/cm^2	Milliwatt per Centimeter Square
min	Minute
%	Percent
λ	Wavelength
n	Refractive Index
k	Extinction Coefficient
∇	Delta
E	Electric Field Vector
π	Pi
k_0	Wavenumber in the Freespace
ϵ_r	Relative Permittivity / Dielectric Constant
Q	Absorbed Power Density
J	Current Density
$\mathbf{E}^*$	Complex Conjugate of the Electric Field
ρ	Material Density
c_p	Specific Heat Capacity
T	Temperature
k	Thermal Conductivity
Q	Thermal Source Term from Electromagnetic Energy Absorption
kg	Kilogram

m	Meter
K	Kelvin
W	Watt
C	Celcius
J	Joule
°	Degree
μs	Microsecond
m	Mass
C	Concentration
V	Volume Containing One Nanoparticle
r	Radius of a Nanoparticle
R	Radius of the Surrounding Medium

LIST OF ABBREVIATIONS

MNP	Melanin Nanoparticle
PTT	Photothermal Therapy
MRI	Magnetic Resonance Imaging
EPR	Enhanced Permeability and Retention
ROS	Reactive Oxygen Species
NIR	Near-Infrared
UV	Ultraviolet
PEG	Polyethylene Glycol
SMNP	Synthetic Melanin Nanoparticles
M@C NP	Melanin Nanoparticles Coated with Cancer Cell Membrane
DOX	Doxorubicin
PDA	Polydopamine
MNP-Fe^{3+}	Fe^{3+} Chelated Melanin Nanoparticle
MNP-Mn^{2+}	Mn^{2+} Chelated Melanin Nanoparticle
PMPDA	Polyethylene Glycol and Mn^{2+}-Chelated Polydopamine
L-DOPA	Mn^{2+} Doped Melanin-Like Poly Nanoparticles
SEM	Scanning Electron Microscope
DLS	Dynamic Light Scattering
FTIR	Fourier Transform Infrared Spectroscopy
UV-Vis	UV-Visible Spectroscopy
FEM	Finite Element Analysis Method
ewfd	Electromagnetic Waves, Frequency Domain
DW	Distilled Water

1. INTRODUCTION

1.1 Motivation and Objectives

The aims of this study are to investigate whether changes in the size of natural melanin nanoparticles (MNPs) and chelation of natural MNPs with Fe^{3+} ions change the photothermal therapy (PTT) efficacy and if so, how. It is aimed to create a valid simulation model for this research and compare the results obtained with the simulation with in vitro experiments.

Melanin, a naturally occurring biopolymer, serves as a pigment and protective agent in organisms such as animals, fungi, and bacteria. In animals, melanin contributes to the coloration of skin, eyes, and hair and to light protection. In fungi and bacteria, it helps to survive by resisting environmental stress. In recent years, naturally or synthetically obtained MNPs have been frequently investigated in biomedical applications such as drug delivery, wound healing, and PTT due to their biocompatibility, antioxidant properties, and light absorption. In addition, the chemical structures of natural and synthetic MNPs allow them to chelate metal ions such as Fe^{3+}, Cu^{2+}, Gd^{3+}, and Mn^{2+}. MNPs exhibit paramagnetic properties, meaning they can be magnetized under a magnetic field. When MNPs are conjugated with Fe^{3+} and Mn^{2+} ions, they can be used as a contrast agent in T1-weighted MR imaging due to their high T1 relaxation times. Thus, these nanoparticles can also be used as contrast agents in magnetic resonance imaging (MRI). There are studies in which MNPs chelated with metal ions are used simultaneously for both imaging and treatment, i.e. theranostic purposes. Theranostic is a term formed by combining the words "therapy" and "diagnostic". Theranostic studies refer to approaches that aim to diagnose and treat the disease simultaneously. The materials or agents used in this approach have properties that will help both diagnose the disease and treat it. Especially in complex diseases such as cancer, theranostic approaches allow the disease to be diagnosed accurately and targeted treatment to be applied simultaneously. If the MNPs conjugated with

metal ions retain their photothermal properties, they can be used as theranostic agents for photothermal cancer treatment under MRI. However, changes in the size of the nanoparticles used, the wavelength of light used during PTT, and the chelated metal ion may have cross-effects in theranostic applications. Differences in the size of MNPs and the wavelength of light used during PTT can change the heat that MNPs will produce as a result of exposure to light. As a result of chelation with metal ions, the electronic configuration, optical properties, thermal conductivity and stability of MNPs can change. This can change the heat that MNPs chelated with metal ions will produce as a result of exposure to light. The increase in the temperature of MNPs chelated with metal ions as a result of PTT application can affect the MRI contrast performance by changing the structure and behavior of these nanoparticles under magnetic fields.

This study aimed to investigate whether changes in the size of MNPs influence the efficiency of PTT and whether chelation of these MNPs with Fe^{3+} ions alters their photothermal performance. Through a combination of computational modeling and in vitro experiments, the research sought to evaluate these effects. The outcomes of this study are expected to contribute to the optimization of melanin-based theranostic platforms by identifying the most effective nanoparticle size, and irradiation parameters for enhancing therapeutic efficacy.

1.2 Organization of Thesis

Chapter 1 introduces the study by outlining its core concept, research motivation, and specific objectives. Chapter 2 situates the research within the existing body of literature and highlights its importance. Chapter 3 details the materials and methods used. Chapter 4 presents the findings of the study. Chapter 5 provides a critical analysis and interpretation of the results in relation to prior studies and offers recommendations for future studies and potential enhancements. Finally, Chapter 6 summarizes the key outcomes of the research.

2. BACKGROUND

2.1 Conventional and Alternative Treatment Methods for Cancer

Cancer is a complex and life-threatening disease that occurs when cells divide and multiply out of control and is affected by genetic and environmental conditions [1]. There are many distinct types of cells that make up the human body. The normal process of cell division in a healthy organism involves the controlled growth, division, death, and replacement of cells [2]. After undergoing DNA alterations, cancer cells begin to divide and proliferate uncontrollably, eventually joining forces to create a mass known as a tumor [3]. Since benign tumors can be created from cells that resemble normal cells but do not proliferate quickly or migrate to other organs, the appearance of a tumor mass in the body does not always indicate the presence of cancer. The altered cells in malignant tumors, on the other hand, proliferate quickly and become cancerous. They can separate from the original tissues and spread to other areas of the body, where they might cause metastases [3, 4].

Conventional treatment modalities for cancer includes chemotherapy, radiation, and surgery. Chemotherapy involves using cytotoxic drugs to target and destroy cancer cells in the body. These medications either kill cancerous cells or slow the growth of them. Chemotherapy is used to totally eradicate the tumor, heal the patient, stop the spread of the tumor, and limit its growth. In some cases, chemotherapy can be given before or after other treatment modalities like surgery or radiotherapy [5, 6]. Radiotherapy uses ionizing radiation to kill cancerous cells and shrink tumors. Radiotherapy can be external, internal, or systemic. External radiotherapy, the most common type, delivers radiation from outside the body. Internal and systemic therapies involve the placement or administration of radioactive material, often requiring hospitalization [7]. Cancerous tissue is removed from the body through surgery. Surgery is frequently the first line of treatment for cancer. The type of surgery performed and the patient's

overall condition before to the procedure will both influence the side effects of the procedure. The most typical adverse effect is pain, which is easily managed in the majority of individuals [8].

Since cancer is a complex disease, these methods are often ineffective in completely treating the disease and the quality of life for patients is greatly impacted by the severe side effects. The severe side effects show how important it is to keep trying to find better ways to treat different kinds of cancer with minimal side effects. PTT stands out as an innovative and promising method in cancer treatment. This method destroys cancer cells by causing light-sensitive nanoparticles to produce heat in the targeted tumor area [9]. While traditional treatment methods can also damage healthy tissues, photothermal therapy reduces the risk of side effects by minimally affecting healthy cells. In addition, since it is not an invasive method, patients' treatment process is more comfortable and the recovery period is shortened.

2.2 Photothermal Therapy (PTT)

PTT is a minimally invasive treatment that uses light-absorbing agents, called photothermal agents, to generate heat that can destroy cancer cells or other abnormal cells in the body. When these agents are exposed to specific wavelengths of light, they enter an excited state and as a result of this activation, they convert the light energy into heat by the emitted vibrational energy. This localized heating effect raises the temperature of the targeted cells, causing cellular damage and ultimately leading to cell death [10].

The majority of materials that are now being researched for PTT are of the nanoscale variety. To support its growth, a tumor needs new blood vessels, which differ from normal blood vessels in that they have poor lymphatic drainage and an unorganized, leaky vasculature. A tumor has a substantially higher concentration of some particles than the rest of the body due to these characteristics [11]. The nanoscale size of these materials allows them to exploit these unique features of tumor vasculature,

leading to a phenomenon known as the enhanced permeability and retention (EPR) effect. This effect enables nanoparticles to passively accumulate within the tumor tissue more effectively than in healthy tissue. As a result, nanoscale particles can deliver therapeutic agents directly to tumor sites with increased precision, minimizing side effects on surrounding healthy cells. This targeted accumulation is a critical advantage in PTT, as it allows for localized heating of the tumor when these particles are activated, potentially enhancing the efficacy of the treatment while sparing healthy tissues from damage [12, 13].

Photothermal agents are light-absorbing materials used in PTT to convert absorbed light typically in the near-infrared (NIR) range into heat. This localized heat generation leads to elevated temperatures in the tumor microenvironment, resulting in cancer cell death through thermal ablation. These agents are often designed to accumulate preferentially in tumor tissues, ensuring selective damage to malignant cells while minimizing harm to surrounding healthy tissue. Common photothermal agents include gold nanostructures, carbon-based materials, and MNPs, each chosen based on their photothermal conversion efficiency, biocompatibility, and optical properties [14]. In this study, MNPs were investigated as photothermal agents for effective cancer treatment using PTT.

2.3 Melanin Nanoparticles (MNPs)

Melanin is a natural pigment found in many living organisms, including humans, animals, plants, and microbes, and acts as an ultraviolet (UV) shielding agent, antioxidant, and structural color element in these living organisms [15]. In humans, melanin is the determinant of skin, hair, and eye color. Increased melanin density means darker skin, hair, and eye color. In humans, it can also be found in the pigmented tissue underlying the iris of the eye, in pigment-carrying neurons in the brainstem regions, and in the inner ear. Other functions in the eye include preventing light from scattering within the retina, providing clearer vision, and protecting the eyes from excess light. Melanin is very important in protecting organisms against environmental factors and

regulating biological functions [16].

MNPs are nanoscale particles composed of melanin, a natural pigment found widely in living organisms, responsible for coloration in skin, hair, eyes, and certain internal tissues. Beyond pigmentation, melanin plays critical biological roles due to its strong broadband absorption, metal ion chelation, free radical scavenging, and photoprotective properties. These characteristics make MNPs highly valuable in various biomedical applications, including drug delivery, bioimaging, antioxidant therapy, and cancer treatment. MNPs can be obtained through two primary sources: natural extraction and synthetic production. Natural MNPs can be produced from various sources such as bacteria, fungi, squid, insects, black tea leaves, octopus, squid, skin and hair by centrifugation and simple washing processes [17–19]. Their main advantages lie in their native biological origin, excellent inherent biocompatibility, and complex polymeric structure, which may confer additional functional groups and biological activity that are difficult to replicate synthetically. Moreover, natural melanin often exhibits intrinsic photothermal and antioxidant activity, making it highly suitable for biomedical use with minimal modification. These properties are especially valuable in applications where safety and physiological compatibility are critical [20]. On the other hand, synthetic MNPs (SMNPs) often based on polydopamine (PDA) are produced via the oxidative polymerization of dopamine under alkaline conditions. While they may lack some of the biological complexity of natural melanin, SMNPs offer precise control over size, morphology, and surface chemistry, and are easier to scale up reproducibly. This tunability makes SMNPs particularly advantageous in advanced applications that require surface functionalization, such as targeted drug delivery or integration with imaging agents (e.g., MRI or photoacoustic contrast). They can be engineered to incorporate pH-responsive or light-sensitive drug release mechanisms and co-loaded with therapeutic agents or photosensitizers for synergistic photothermal and photodynamic therapy. Furthermore, SMNPs can be customized for multi-modal imaging via metal ion chelation (Fe^{3+}, Mn^{2+}, Gd^{3+}), expanding their use in theranostic platforms [21]. While both natural and synthetic MNPs share many core properties, natural MNPs are superior in terms of native biocompatibility, lower immunogenicity, and intrinsic biological functionality, making them ideal for translational and in vivo applications. Synthetic

MNPs, meanwhile, offer enhanced design flexibility and scalability for multifunctional nanoplatforms. The choice between them depends on the intended application.

MNPs have a wide potential in biomedical research and applications, and offer innovative solutions especially in the fields of medical diagnosis, treatment and protection. They can be used to carry drugs and provide controlled drug release. Since they have a strong antioxidant effect against oxidative stress, they are used in the fight against aging and diseases by protecting cells from free radicals. This allows drugs to be delivered directly to diseased cells in targeted therapies such as cancer treatment. MNPs absorb light of certain wavelengths and convert it into heat. This property is used in photothermal treatment methods targeting cancer cells, destroying cancer cells by using the heat generated from light absorption. There are studies in the literature on the use of MNPs as photosensitizers in photothermal treatment of cancer. Recently, it has also attracted attention as an environmentally friendly alternative to metallic and metal oxide nanoparticles in biosensors and bioelectronic applications [22–25].

MNPs exhibit paramagnetic properties, meaning they can become magnetized when under a magnetic field. This property can shorten the T1 relaxation time of surrounding protons. This causes melanin-containing tissues to appear brighter on T1-weighted MR images [26]. Since MNPs or tissues with high melanin content (e.g. melanomas) shorten the T1 relaxation time, these tissues show increased signal on T1-weighted MR images [27]. In other words, these tissues become brighter and more distinct. Therefore, MNPs can also be used as contrast agents to improve image quality in medical imaging techniques [28]. Studies in the literature have also shown that natural MNPs conjugated with metal ions can also serve as contrast agents for T1-weighted MR due to their high T1 relaxation times.

There are many studies in the literature where MNPs are used as an effective agent in photothermal treatment of cancer [18]. In the study conducted by Kim et al., MNPs were conjugated with polyethylene glycol (PEG) in order to increase the biocompatibility of MNPs [29]. As a result of this conjugation process, melanin-PEG conjugates that self-assembled to form stable nanoparticles were obtained. Thanks to

their characteristic photothermal properties, MNPs showed high photothermal conversion efficiency in the form of melanin-PEG nanoparticles both in vitro and in vivo. In the study, melanin-PEG nanoparticles were injected intravenously into the tail vein of mice carrying 4T1 tumors and then exposed to NIR light source beam at a wavelength of 808 nm and a power density of 1.5 W/cm^2. As a result of this application, the temperature in the tumor region increased to 48°C and tumor growth in the treatment group decreased by 50% compared to the control group. The findings show that melanin-PEG nanoparticles effectively suppress tumor growth under NIR light source irradiation after intravenous administration and are a strong candidate for photothermal therapy. In another study, Li et al. designed a photothermal and immune co-therapy strategy based on natural MNPs for the treatment of breast cancer [30]. Natural MNPs produced from cuttlefish were used as photothermal reagents by coating them with a cancer cell membrane (M@C NP) to ensure homologous adhesion of tumors. The resulting M@C NPs exhibited much improved antitumor activity. This integrated strategy based on natural MNPs resulted in increased numbers of CD8+ T cells and higher cytokine levels, thus enabling effective treatment of primary and abscopal tumors. In the study conducted by Liu et al., PDA-DOX nanoparticles, a natural product used in chemotherapy drug loading, were developed to enhance the effect of doxorubicin (DOX), a chemotherapy drug. The PDA used in the study, namely polydopamine, is an MNP analog. In addition to detecting the great stability and robust biocompatibility of the natural product, the strong photothermal conversion ability and simultaneous Reactive Oxygen Species (ROS) production effect, which are suitable for phototherapy, were also exhibited. Considering this; PDA-DOX and appropriate in vitro NIR irradiation showed good synergistic chemotherapy/PTT effects against OS-RC-2/ADR cells compared with PDA containing DOX or NIR alone. As a result, it was concluded that PDA-DOX may be an effective drug for renal carcinoma chemotherapy and phototherapy and can be used for tumor immunotherapy [31]. Magnetic resonance imaging (MRI) has many advantages compared to X-ray-based imaging methods due to its working principle that does not include ionizing radiation, provides high soft tissue contrast, and provides physiological data such as temperature, pressure, perfusion, and diffusion in addition to anatomical information about tissues [32, 33]. Gadolinium (Gd^{3+})-containing contrast solutions are frequently used today to increase

the visibility of the relevant tissue and organ under the MRI scanner and to increase diagnostic accuracy. However, as a result of the high toxicity rates of Gd^{3+}-containing contrast solutions, the search for new MRI contrast agents with high biocompatibility has attracted the attention of researchers [34]. For this purpose, Chen et al. and Ju et al. in two separate studies, in vitro and in vivo biocompatibility and biodegradability tests were performed on MNPs attached to various metal ions (Copper (Cu^{2+}), Iron (Fe^{3+}), Manganese (Mn^{2+})) and they showed that metal ion-chelated MNPs have negligible low toxicity and high biodegradability [35]. Baysoy and his colleagues, who are researchers in this project, compared the contrast properties of Fe^{3+} chelated MNPs (MNP-Fe^{3+}) with the commercially available Gd^{3+} contrast agent (Gadobutrol Monohydrate, Sigma-Aldrich) at the same concentrations in a study and showed that MNP-Fe^{3+} had a higher T1-shortening effect and a higher signal-to-noise ratio in the MRI scanner than Gd^{3+} [36, 37]. Baysoy et al. in another study, coated Mn^{2+}-chelated MNPs (MNP-Mn^{2+}) on MR-compatible guidewires to develop a guidewire prototype that can be used for interventional surgeries guided by MR imaging and provided bright visualization of the guidewires with high contrast under MR [38]. In summary, MNPs chelated with Fe^{3+}, Cu^{2+}, Mn^{2+} and similar metal ions provide high signal (positive contrast) by providing short T1 relaxation times in images taken with an MR scanner. Considering this feature, in addition to their high biocompatibility and biodegradability, metal ion-chelated MNPs are emerging as an alternative contrast agent in diagnostic and therapeutic clinical applications applied in MR scanners.

There are also theranostic studies in which melanin and melanin-like nanoparticles are used simultaneously for PTT and MRI. For example, Miao et al. designed PEG and Mn^{2+}-chelated polydopamine (PMPDA) nanoparticles to increase MR imaging signals and kill cancer cells with photothermal therapy. These nanoparticles created high contrast under 9.4 T MR device, and the photothermal therapy effect they produced as a result of applying 808 nm wavelength light source at 2 W power for 10 minutes was shown on HeLa cells [39]. Kang et al. In another study conducted by , Mn^{2+} doped melanin-like poly(L-DOPA) nanoparticles sensitive to near-infrared light, which serve as multifunctional nanoplatforms in cancer treatment, were designed and it was shown that these nanoparticles can be used as a platform combining photother-

mal, photodynamic and chemotherapeutic effects, providing both T1-weighted MRI contrast and being effective in targeted drug delivery and tumor ablation [40]. Dong et al. used polydopamine (PDA) nanoparticles, which they synthesized as a melanin-like polymer, as a platform that can load multiple therapeutic and imaging agents, and successfully achieved a combination of chemotherapy and PTT under MRI guidance with this system [41].

All these studies show that MNPs are a versatile tool that can be used in both imaging and therapeutic applications. However, cross-effects such as how the nanoparticle size and the wavelength of light used change the PTT efficiency, the effect of chelation of MNPs with metal ions for such theranostic applications on PTT performance, and the effect of increasing the temperature during PTT in terms of MR contrast have not been investigated before. This study investigated these effects with modeling and in vitro experiments, and enabled the determination of the most appropriate nanoparticle size and metal ion for theranostic applications with MNPs.

3. MATERIALS AND METHODS

3.1 Synthesis of Nanoparticles

A collaboration was made with Bahçeşehir University, Faculty of Engineering and Natural Sciences, Department of Biomedical Engineering and İzmir Democracy University, Faculty of Engineering, Department of Biomedical Engineering for the production of natural MNPs and their Fe^{3+} conjugates.

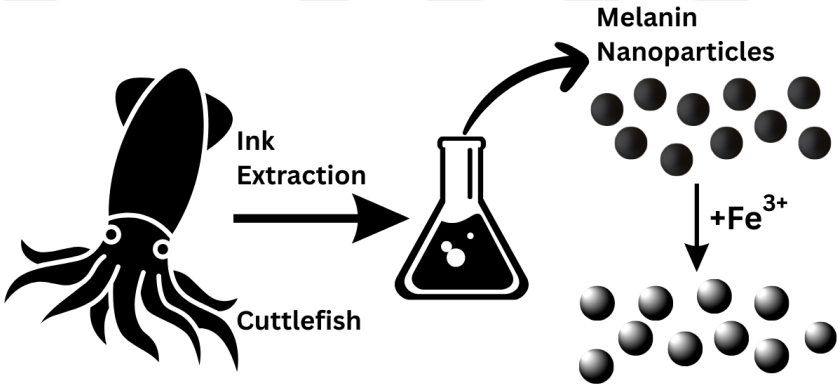

Figure 3.1 Synthesis of MNPs and MNP-Fe^{3+}s from cuttlefish ink.

Freshly dissected cuttlefish (Sepia officinalis) ink sacs were used to extract natural MNPs in accordance with the method shown in the literature [42]. Following three repetitions of washing and centrifuging at 10,000 rpm for 20 minutes, the MNPs were re-dispersed in water using an ultrasonic bath. Fe^{3+} ion chelation with MNPs was facilitated by a straightforward mixing procedure. In particular, a 100:1 (v/v) ratio was used to combine a solution of MNPs (1 mg/mL) with a solution of Fe^{3+} (1 mg/mL). To eliminate any free Fe^{3+} ions, the mixture was then centrifuged at 10,000 rpm. To ascertain the Fe^{3+} content in the MNPs, the supernatant was collected using a membrane filter with a pore size of 0.45 μm for measurement by inductively coupled plasma mass spectrometry (ICP-MS) using a Perkin-Elmer Optima-5300-DV. Using SEM, the impact of Fe^{3+} chelation on the MNPs' morphology was observed [38]. The obtained nanoparticles were diluted with distilled water at concentration of 0.2 mg/mL and for use in the experiments.

3.2 Characterization of Nanoparticles

Scanning Electron Microscope (SEM) and Dynamic Light Scattering (DLS) characterization methods were used to determine the nanoparticle size and morphology. The chemical structures of the nanoparticles were analyzed with Fourier Transform Infrared Spectroscopy (FTIR). These analyses was performed with the service of Boğaziçi University Life Sciences Center. Finally, the absorbance spectra of the nanoparticles was measured with Nanodrop 2000c UV-Vis spectrophotometer. Each characterization method was performed once for the analysis of the nanoparticle samples.

SEM was used to characterize the MNPs and MNP-Fe^{3+}s morphologically. 10 mg/mL solutions were diluted with with 1 mL distilled water. The nanoparticle solutions were drop-cast onto a conductive carbon tape or a clean silicon wafer and allowed to cure at room temperature for 3 hours before imaging. After that, the prepared samples was put inside the SEM chamber one-by-one, and imaging was done with an accelerating voltage of 30 kV while under high vacuum. The produced nanoparticles' shape, surface texture, and particle size were all thoroughly described by the obtained SEM pictures.

Using DLS, the size distribution and hydrodynamic diameter of the produced nanoparticles were ascertained. 10 mg/mL solutions were diluted with with 1 mL distilled water. To guarantee a uniform dispersion and reduce particle agglomeration, the nanoparticle suspensions were placed in ultrasonic bath for 30 minutes before measurement. At a given angle, variations in the intensity of scattered light resulting from the Brownian motion of the nanoparticles were observed during the analysis, and the Stokes-Einstein equation was used to compute the particle size distribution. The findings, which showed the homogeneity of the nanoparticle population, were presented as intensity-based average diameters and the polydispersity index (PDI).

The molecular structure and functional groups found on the surface of MNPs and MNP-Fe^{3+}s were examined using FTIR analysis. By monitoring the absorption of infrared radiation at different wavelengths that correspond to vibrational transitions

of molecular bonds, this approach makes it possible to identify certain chemical bonds and interactions. The FTIR spectra used in this study was captured between 4000 and 400 cm^{-1}. To create pellets appropriate for transmission-mode measurements, the nanoparticle samples were first dried and crushed with potassium bromide (KBr). The presence of functional groups like hydroxyl (-OH), amine (-NH_2), carbonyl (C=O), and aromatic rings, all of which are frequently linked to melanin structures, were determined by analyzing characteristic absorption peaks. The identification of spectrum shifts or intensity changes suggestive of metal-ligand interactions was made possible by comparing MNPs with MNP-Fe^{3+}s. Specifically, changes in the C=O or C=C bands and the large -OH/NH stretching area demonstrated effective iron chelation. The efficient incorporation of Fe^{3+} ions into the nanoparticle matrix and the structural integrity of melanin were therefore qualitatively confirmed by the FTIR study.

MNPs and MNP-Fe^{3+}s' optical absorbance properties were assessed with a Nanodrop 2000c UV-Vis spectrophotometer (Thermo Fisher Scientific, USA). The purpose of this analysis was to ascertain how the nanoparticles absorbed light at various wavelengths and to look into whether they would work well as photothermal agents. In order to guarantee uniform dispersion, nanoparticle solutions were prepared at a concentration of 50 μg/mL in distilled water and kept in ultrasonic bath for 30 minutes before testing. Every sample was put straight onto the spectrophotometer's microvolume pedestal, and absorbance spectra were taken at room temperature between 300 and 900 nm. Due to the deeper tissue penetration of NIR light, the acquired spectra showed broad and monotonic absorbance patterns, especially extending into the NIR region, which is beneficial for PTT applications. The optical characteristics of the nanoparticles were assessed using the spectrum shape and absorbance intensity. In particular, at phototherapeutically important wavelengths (e.g., 530 nm, 633 nm, and 785 nm), comparisons between MNPs and MNP-Fe^{3+}s revealed possible shifts or increases in absorbance, indicating better photothermal conversion potential upon metal ion chelation. Thus, UV-Vis spectroscopy gave important information about how the nanoparticles interact with light, which is directly related to how well they work as photothermal transducers in biomedical applications.

3.3 Simulation of the Effect of Melanin Nanoparticle Sizes and Light Used in PTT on Temperature Increase

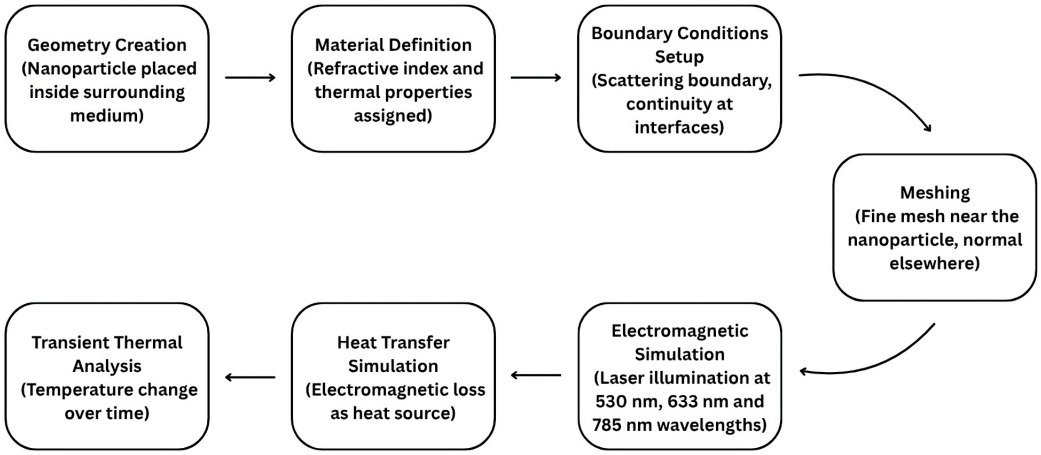

Figure 3.2 Simulation workflow.

COMSOL Multiphysics® simulation software was used to simulate MNP excitation with light sources. COMSOL Multiphysics® simulation software is used in engineering, industry and scientific research. The software includes fully coupled multiphysics and single physics modeling capabilities as well as tools for developing simulation applications. COMSOL, which works based on finite element analysis method (FEM), is a simulation software developed with real-world applications in mind. The stated goal of the simulation is to mimic the effects observed in reality as accurately as possible. Models should be in the context of engineering or science. This necessitates the use of more than one physiology. Modeling examples of this simulation program include acoustics, electromagnetics, chemical reactions, mechanics, fluid motion and heat transfer. Since all these effects are present in the real world, they should also be present in the simulation environment [43]. In addition to the main software called the core product in the program; there is an additional module that were purchased and used within the scope of the requirements of the model to be designed. In this study, the "Heat Transfer in Solids" module was also used in addition to COMSOL Multiphysics® software. The variables related to the required dimensions and chemical properties of the MNPs produced were determined in the software from every aspect and the geometric model design was created. Then, the energy parameters needed in

the PTT phase were determined using the "Heat Transfer in Solids" module. FEM was followed in the computational modeling phase. After that, temperature maps and written information were obtained regarding how much temperature increase was observed on the nanoparticles.

For the simulation to be carried out, the physical and chemical properties of the nanoparticles were defined. While creating the geometry, nanoparticles and biological environment were modeled, and then light source radiation effects were analyzed. The nanoparticle size was determined as 150 nm and shape as spherical in accordance with the real properties that were determined in the characterization phase with SEM. To mimic the environment of nanoparticles dissolved in distilled water, the surrounding medium was determined to be distilled water. During in vitro experiments, when exciting MNPs with light source, the distance of the light source to the solution in the plate was calculated and the height of the model was created accordingly. Thermal conductivity, optical absorption and diffusion variables of the simulation environment were determined. Light source radiation with wavelengths of the visible range was defined for modeling photothermal effects; optical energy conversion of nanoparticles and the resulting heat transfer was examined by considering the power density and energy absorption of these light sources.

In simulation projects conducted using COMSOL Multiphysics®, the initial step involves defining the spatial dimensions of the study. The spatial dimensions was defined as 3D. The physics interface of the study was determined as Electromagnetic Waves, Frequency Domain. Time-harmonic electromagnetic field distributions are solved using the Wave Optics, Electromagnetic Waves, Frequency Domain interface. The study was determined as Frequency Domain. The response of a linear or linearized model to harmonic excitation for one or more frequencies is calculated using the frequency domain study [44].

3.3.1 Design and Geometry

In the characterization phase of the methodology, MNPs were determined to have a radius of 75 nm. For the experimental study, MNPs were dissolved in distilled water, and 2 mL of the solution was placed in a well of a 24-well plate, followed by irradiation with 530 nm, 633 nm and 785 nm light sources for 30 minutes. To computationally replicate these conditions, a simulation study was conducted, wherein a 75 nm radius sphere (representing the nanoparticle) was positioned at the center of a larger spherical domain with a radius 20 times greater (modeling the surrounding medium). The radius of the surrounding medium was determined based on the volume that would contain a single melanin nanoparticle of radius 75 nm.

The mass m of a single nanoparticle was determined using the spherical volume formula given in Eq. 3.1 and the bulk density of melanin ($\rho = 1.5\,\mathrm{g\,cm^{-3}}$).

$$m = \frac{4}{3}\pi r^3 \rho\,, \tag{3.1}$$

where r is the nanoparticle radius.

Given the experimentally measured concentration C, the volume V containing one nanoparticle was derived with the formula given in Eq. 3.2.

$$V = \frac{m}{C}\,. \tag{3.2}$$

The equivalent spherical radius R of the surrounding medium corresponding to this volume was then calculated by Eq. 3.3.

$$R = \left(\frac{3V}{4\pi}\right)^{1/3} . \tag{3.3}$$

The ratio of the medium radius R to the nanoparticle radius r was evaluated as Eq. 3.4.

$$\frac{R}{r} \approx 19.2 . \tag{3.4}$$

To match experimental conditions, the simulation domain was scaled such that the surrounding medium extended to a radius $R \approx 19.2r$, ensuring accurate representation of the nanoparticle concentration. This approximate value was defined as 20 in the simulation.

The simulated results were then compared with experimental findings to validate the study. The geometric design is presented in Figure 3.4.

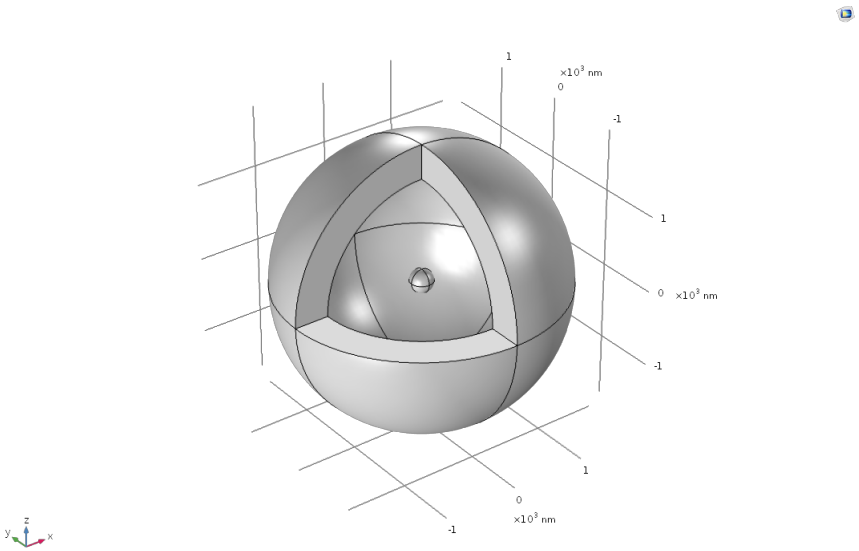

Figure 3.3 Geometry of the MNP.

3.3.2 Definition and Calculation of Material and Electrical Properties

The material definition requires specification of the complex refractive index of MNPs, comprising both real and imaginary components. The wavelength-dependent refractive index profile for MNPs, as documented in the literature, is presented in Figure 3.5.

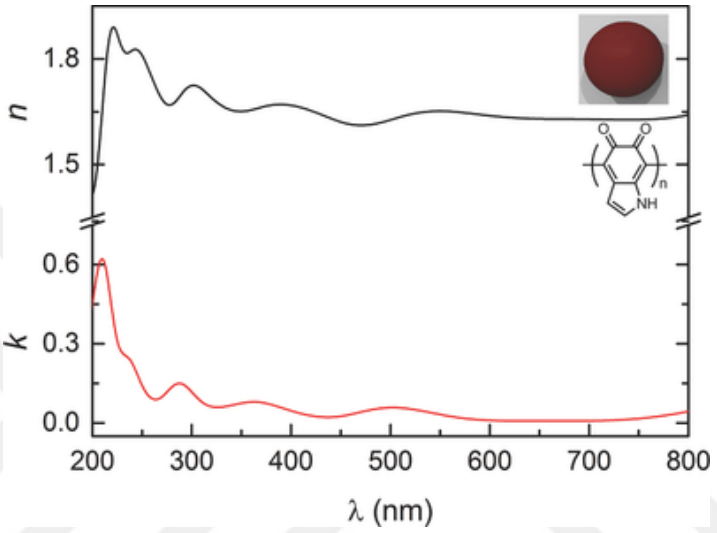

Figure 3.4 Ellipsometric characterization of melanin. Refractive index n (black) and extinction coefficient k (red) determined via variable angle spectroscopic ellipsometry [45].

The complex refractive index (n + ik) values for the nanoparticle were taken from the literature and assigned to the model. Here, n represents the real refractive index and k represents the extinction coefficient. The correct definition of these parameters is critical for the correct modeling of the heat generation resulting from the interaction of the nanoparticle with the light source beam. The refractive index of the solution (medium) was fixed as n = 1.33, which is the standard value for distilled water [46].

In the model separate analyses were performed for the target wavelengths of 530 nm, 633 nm and 785 nm. The power of the light source used was determined as 100 mW/cm^2 and the input intensity was modeled accordingly. The complete set of defined optical parameters are presented in Table 3.1.

Table 3.1
Refractive index n and extinction coefficient k of MNP for the specified wavelengths.

Wavelength (nm)	n_{MNP}	k_{MNP}
200	1.8	0.6
220	1.6	0.3
250	1.7	0.1
300	1.6	0.2
350	1.65	0.1
400	1.6	0.05
450	1.6	0.02
500	1.6	0.01
550	1.6	0.005
600	1.6	0.002
650	1.6	0.001
700	1.6	0.0005
750	1.6	0.0002
800	1.6	0.0001

Eq. 3.5 was used for the electromagnetic wave solution.

$$\nabla \times \nabla \times \mathbf{E} - k_0^2 \epsilon_r \mathbf{E} = 0 \tag{3.5}$$

where:

- k_0 is the wavenumber in free space, defined by Eq. 3.6.

$$k_0 = \frac{2\pi}{\lambda} \tag{3.6}$$

  with λ being the wavelength of the electromagnetic wave,

- ϵ_r represents the relative permittivity (or dielectric constant), calculated using the complex refractive index $\tilde{n} = n - ik$ as given in Eq. 3.7.

$$\epsilon_r = \tilde{n}^2 = (n - ik)^2 = (n^2 - k^2) - i(2nk) \tag{3.7}$$

  where n is the refractive index and k is the extinction coefficient.

Using the refractive index, the relative dielectric constant of the material was calculated with Eq. 3.8.

$$\epsilon_r = (n + ik)^2 \tag{3.8}$$

Following the definition of these electromagnetic parameters, the electromagnetic power loss following the electromagnetic field calculations, the absorbed power density (Q) was determined through the electromagnetic work done on the system. The power dissipation was computed with Eq. 3.9.

$$Q = \frac{1}{2}\Re(\mathbf{J} \cdot \mathbf{E}^*) \tag{3.9}$$

where $\mathbf{J}$ is the current density and $\mathbf{E}^*$ represents the complex conjugate of the electric field. This quantity serves as the thermal source term for subsequent coupled multiphysics analysis.

As a result, the electromagnetic absorption profile formed inside the nanoparticle was extracted and this profile was transferred to the heat transfer module and the time-dependent change of the temperature distribution was calculated.

3.3.3 Definition of Boundary Conditions

In the model, the "Scattering Boundary Condition" was applied at the boundaries of the large sphere representing the external environment. This boundary condition was used to accurately represent the scattering of light source light outside the system and allows avoiding artificial reflections.

In the inner regions, a continuous boundary condition was used at the interfaces of the nanoparticle and the medium. This condition ensured the continuity of the electric and magnetic field components, ensuring that the interactions between the nanoparticle and the medium were in accordance with physical reality.

3.3.4 Definition of Mesh Structure

In order to increase simulation accuracy and optimize solution time, an adaptive mesh structure was used in the model. Types of the elements were defined as free tetrahedral and free triangular. A finer mesh was applied on the surface of the nanoparticle and in the regions exposed to the light source beam. A normal mesh was preferred in the remote regions of the medium in order to reduce the solution cost. Especially due to the small size of the nanoparticle, the minimum element size was set to be one tenth of the wavelength ($\approx \lambda/10$) for the correct resolution of the electromagnetic field gradients around the particle.

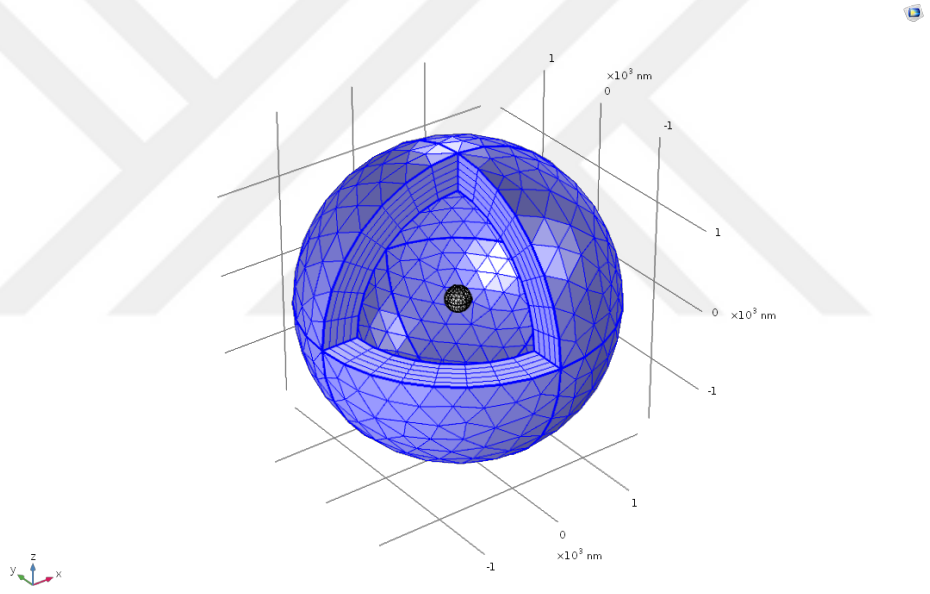

Figure 3.5 PML surrounding a nanosphere for domain truncation in calculations.

3.3.5 Thermal Analysis and Energy Transfer

The power loss distribution obtained with the electromagnetic module was transferred to the "Heat Transfer in Solids" physics interface as a heat source. The heat transfer process is managed by the transient thermal conduction equation given in Eq. 3.10.

$$\rho c_p \frac{\partial T}{\partial t} = \nabla \cdot (k \nabla T) + Q \tag{3.10}$$

where:

- ρ: Material density (kg/m^3),
- c_p: Specific heat capacity (J/kg·K),
- T: Temperature (K),
- k: Thermal conductivity (W/m·K),
- Q: Thermal source term from electromagnetic energy absorption (W/m^3).

Material properties (density, specific heat capacity, thermal conductivity coefficient) were determined according to literature data [47] and assigned to the model. The ambient temperature was entered as 25°C as the initial condition, and the system was provided with self-heating by releasing thermal flux at the edges (thermal insulation).

To accurately model the behavior of nanoparticles in varying environments, simulations were conducted in two distinct media: water and blood. These simulations aimed to represent the dispersion of melanin nanoparticles within both distilled water and blood environments. The specified material properties of MNPs, distilled water and blood are presented in Table 3.2.

Table 3.2
Physical properties of MNP dispersions in various media.

Parameter	MNP	Distilled Water	Blood
Density (kg/m^3)	1450	1000	1055
Thermal Conductivity (W/(m.K))	0.25	0.6	0.5
Heat Capacity at Constant Pressure (J/(kg.K))	1400	4180	3750

The simulation was performed with a transient (time-dependent) solution to examine how the temperature change evolved over time during exposure to the light sources with different wavelenghts.

3.4 Simulation of How MNPs Chelated with Fe^{3+} Ions Effect PTT Efficiency

For the simulation of how MNPs chelated with metal ions effect PTT efficiency, the physical and chemical properties of the nanoparticles were defined. These properties include nanoparticle size, shape and the thermal and optical properties imparted by Fe^{3+} ions after chelation. Thermal conductivity, optical absorption and diffusion variables of the simulation environment were determined. In this study, COMSOL's "Heat Transfer in Solids" module was used. While creating the geometry, nanoparticles and biological environment were modeled, and then light source radiation effects were analyzed. The nanoparticle size defined in accordance with the real properties obtained from SEM analysis. Light source radiation with wavelengths of the visible range was defined for modeling photothermal effects; optical energy conversion of nanoparticles and the resulting heat transfer was examined by considering the power density and energy absorption of these light sources. A time-dependent analysis was performed during the simulation and both temperature increase and thermal distribution were evaluated. The effects of Fe^{3+} ions on the optical and thermal properties of nanoparticles were compared and the outputs such as temperature distribution and maximum temperature increase were visualized. The obtained results were compared with the experimental data to evaluate the accuracy of the model and the effects of the specified metal ions on photothermal activity were analyzed.

3.4.1 Design and Geometry

To investigate the effect of Fe^{3+} ion chelation on the photothermal performance of MNPs, a computational model was constructed using COMSOL Multiphysics®.

From SEM analysis it was obtained that after Fe^{3+} ion chelation, MNP size didn't change. Therefore, a 150 nm spherical domain was designed to represent a single MNP chelated with Fe^{3+} ions. This domain captures the localized light-matter interactions and heat generation. The nanoparticle was placed inside a larger spherical domain, mimicking the surrounding environment of distilled water, to simulate realistic boundary interactions and thermal dissipation. By separating the nanoparticle and the medium into distinct domains, it was possible to accurately define their individual optical and thermal properties, as well as to monitor the spatial distribution of the electromagnetic fields and temperature changes during light source irradiation.

3.4.2 Definition and Calculation of Material and Electrical Properties

The optical properties of the Fe^{3+}-chelated MNPs were defined based on experimental data and literature reports indicating enhanced absorption in the NIR region due to metal ion chelation [48]. For the surrounding medium, the standard refractive index of distilled water was applied as 1.33 in the visible and NIR range. Thermal properties were defined separately for each domain. Density, thermal conductivity, and specific heat capacity values of MNP-Fe^{3+} were chosen to reflect their higher heat conversion potential compared to natural unchelated MNPs [49]. For distilled water, known thermal parameters were utilized. The chelation with Fe^{3+} ions is known to increase the optical absorption efficiency of melanin, particularly under NIR light, thereby improving the conversion of absorbed electromagnetic energy into heat [50].

3.4.3 Electromagnetic Wave Simulation

The Electromagnetic Waves, Frequency Domain (ewfd) physics interface was used to simulate the interaction of the light source radiation with the nanoparticle-water system. Light sources were set at wavelengths of 530, 633 and 785 nm and power of 100 mW/cm^2. The surrounding boundary of the external domain was assigned scattering boundary conditions to allow for realistic modeling of light exiting

the computational domain without reflections. The key output of this step was the electromagnetic power loss density (Q_{abs}), representing the spatial distribution of absorbed energy that would subsequently be converted into heat.

3.4.4 Heat Transfer Coupling

The "Heat Transfer in Solids" module was coupled with the electromagnetic simulation to model the thermal effects induced by light source absorption. The absorbed electromagnetic energy was directly introduced as a volumetric heat source in the thermal model. Detailed thermal properties were assigned for both the nanoparticle and the surrounding medium to ensure realistic heat conduction, storage, and dissipation behavior. Convective boundary conditions were applied at the outer surface of the water domain, allowing the simulation of heat loss to the environment, which is critical for mimicking experimental conditions. The simulation accounted for the transient (time-dependent) temperature evolution to capture the dynamic heating profile during continuous light source exposure.

To accurately model the behavior of nanoparticle in varying environments, simulations were conducted in two distinct media: water and blood. These simulations aimed to represent the dispersion of MNP-Fe^{3+} within both distilled water and blood environments. The parameters defined for different environments in the simulation are presented in Table 3.3.

Table 3.3
Physical properties of MNP-Fe^{3+} dispersions in various media.

Parameter	MNP-Fe^{3+}	Distilled Water	Blood
Density (kg/m^3)	1600	1000	1055
Thermal Conductivity (W/(m.K))	0.35	0.6	0.5
Heat Capacity at Constant Pressure (J/(kg.K))	1600	4180	3750

3.4.5 Study Sequence and Result Evaluation

In this simulation, a two-step coupled study approach was applied to accurately model the photothermal response of MNP-Fe^{3+}. First, a steady-state electromagnetic simulation was conducted using the Electromagnetic Waves, Frequency Domain (ewfd) interface to calculate the distribution of the electromagnetic fields and the corresponding energy absorption within the domains when irradiated by the light source at specified wavelengths. The resulting absorbed power density served as the input for the subsequent thermal simulation. Following this, a time-dependent heat transfer simulation was performed using the "Heat Transfer in Solids" module, where the absorbed electromagnetic energy was treated as a volumetric heat source. This allowed the calculation of the dynamic temperature profile within the nanoparticle and the surrounding medium during light source exposure. The outer boundary conditions were defined to simulate convective cooling, ensuring realistic heat dissipation to the environment. By analyzing the temporal and spatial temperature distributions obtained from the simulation, the photothermal conversion efficiency of Fe^{3+}-chelated MNPs was evaluated and compared to that of unchelated MNPs, providing quantitative insights into the enhancement effect of Fe^{3+} chelation.

In the study, two separate simulation models were constructed to investigate the effect of Fe^{3+} ion chelation on the photothermal efficiency of MNPs. While the overall geometry and boundary conditions were kept identical between the two models to ensure a fair comparison, the material properties particularly the optical characteristics were distinct.

In the simulation model representing non-chelated MNPs, the refractive index and absorption properties were based on standard melanin data available in the literature. Melanin naturally exhibits strong broadband absorption, but its absorption efficiency in the NIR region, which is critical for photothermal therapy applications, is moderate. In contrast, the simulation model of MNP-Fe^{3+} incorporated modified optical properties. Chelation with Fe^{3+} ions is known to enhance the electronic conjugation within melanin structures [48], resulting in significantly increased absorption

in the NIR range. Therefore, in this model, the refractive index and absorption coefficients were updated to reflect this enhancement. As a result of these differences, the electromagnetic wave simulation step demonstrated a notably higher absorption density within the MNP-Fe^{3+}s compared to the non-chelated MNPs under identical irradiation conditions (wavelengths of 530 nm, 633 nm and 785 nm with 100 mW/cm^2 light source power). This enhanced absorption directly translated into a greater volumetric heat generation in the thermal simulation phase.

In summary, the primary difference between the two simulations lies in the optical absorption efficiency and the resulting thermal response. Chelation with Fe^{3+} ions enhances the nanoparticle's light absorption capacity in the NIR region, leading to more effective heat generation and higher temperature elevations during light source exposure.

3.5 Excitation of MNPs with 530 nm, 633 nm and 785 nm Light Sources and Comparison of Results with Thermocouple

Natural MNPs used in this study were supplied within the scope of a collaborative agreement with Bahçeşehir University, Faculty of Engineering and Natural Sciences, Department of Biomedical Engineering. The nanoparticles included two distinct groups: natural MNPs and MNPs chelated with Fe^{3+} ions (MNP-Fe^{3+}s). Each solution was prepared by dissolving the materials in distilled water to achieve a concentration of 0.2 mg/mL. The solutions were prepared using an ultrasonic bath (Branson SFX550) to ensure uniform dispersion of the nanoparticles and prevent aggregation that could affect the accuracy of photothermal measurements. For both samples (MNP and MNP-Fe^{3+}), experiments at all wavelengths were conducted in triplicate to ensure reproducibility and reliability of the results.

Following the preparation of homogeneous suspensions, each nanoparticle solution was irradiated with light sources operating at wavelengths of 530 nm, 633 nm and

785 nm, selected based on their relevance within the biological transparency window and the optimal absorption characteristics of melanin-based materials. The output power of the light sources was calibrated to maintain a consistent power density of 100 mW/cm^2 across the irradiated surface. Each experiment was carried out for a duration of 30 minutes under controlled ambient conditions to minimize external temperature fluctuations. The thermal response of the nanoparticle solutions under excitation was continuously monitored using a thermometer device (Voltcraft DT-300) equipped with fine thermocouple probes capable of detecting small temperature changes. Temperature readings were recorded systematically every 2.5 minutes to accurately capture the kinetics of the heat generation process. To account for the intrinsic heating effects of light source irradiation in the absence of nanoparticles, control experiments were conducted in which pure distilled water was exposed to identical light source irradiation conditions. The temperature data obtained from these control experiments served as a baseline, allowing for the discrimination between the thermal contributions due to direct medium absorption and the enhanced photothermal effects resulting from nanoparticle-mediated energy conversion. The collected temperature profiles were subsequently analyzed and compared across all experimental groups. The photothermal activities of MNP and MNP-Fe^{3+} samples were evaluated based on the magnitude and rate of temperature increase. In addition, the experimental results were cross-referenced with numerical simulation data generated using COMSOL Multiphysics® software. In these simulations, the photothermal behavior was modeled under similar boundary conditions and irradiation parameters. By correlating the experimental temperature rises with the simulation outputs, a comprehensive understanding of the photothermal conversion efficiencies of the different nanoparticle formulations was achieved, particularly highlighting the impact of metal ion chelation on enhancing the photothermal performance of melanin-based nanoparticles.

4. RESULTS

This section presents the experimental results and photothermal modeling of MNPs and MNP-Fe^{3+}s. The primary objective of this study was to investigate the effects of Fe^{3+} chelation on the photothermal performance of MNPs under light source irradiation at three distinct wavelengths: 530 nm, 633 nm, and 785 nm. The results are presented beginning with the characterization findings, followed by the simulation outcomes, the experimental data, and lastly with a comparative analysis of the two approaches.

4.1 Synthesis and Characterization of MNPs

In this study, the structural and optical properties of MNPs and MNP-Fe^{3+}s were comprehensively investigated using multiple characterization techniques, DLS, FTIR, UV-Vis, and SEM. These analyses enabled the determination of morphological and chemical differences between MNPs and MNP-Fe^{3+}s, while also providing insights into structural integrity and surface modification potential.

4.1.1 Size and Distribution Analysis by DLS

The DLS analysis revealed small size differences between MNPs and MNP-Fe^{3+}s. Size-intensity distribution comparison of MNPs (blue solid line) and MNP-Fe^{3+}s (red dashed line) are presented in Figure 4.1.

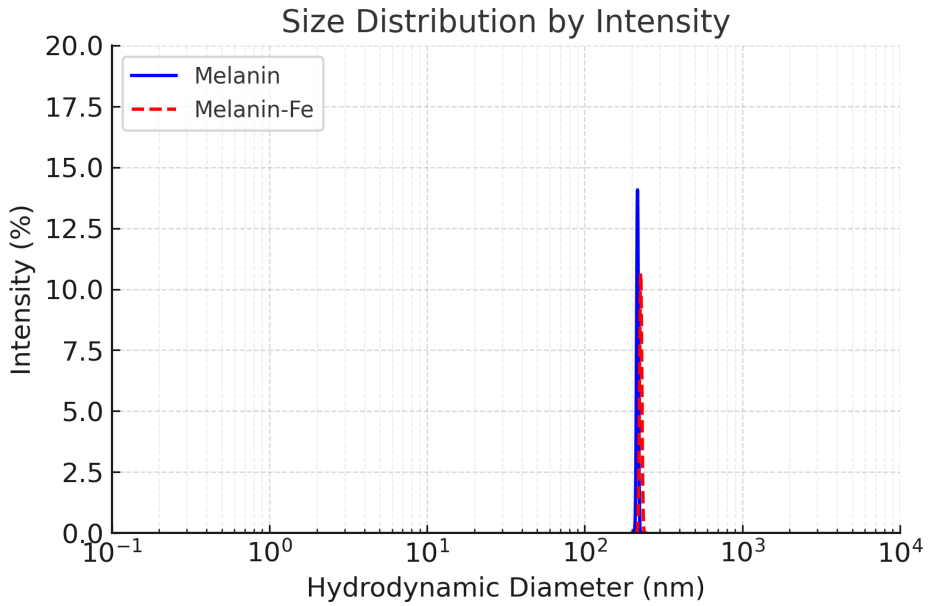

Figure 4.1 Size-intensity distribution comparison of MNPs and MNP-Fe^{3+}s.

Both samples exhibit a narrow, monomodal size distribution on a logarithmic diameter scale. MNP-Fe^{3+}s show a slightly larger peak diameter (226 nm) compared to the MNPs (216 nm), indicating a modest increase in hydrodynamic size upon iron chelation. The Y-axis (Intensity %) is normalized to 100%, and both distributions are sharply peaked (low polydispersity), with the MNP-Fe^{3+} curve slightly broader and lower in peak intensity due to its marginally higher polydispersity. The X-axis is logarithmic (0.1-10,000 nm) as in the original DLS plots, and the Y-axis shows the relative scattering intensity percentage. Error bars are not shown since the data are from single DLS measurements; however, the clear single-peak profiles and the 10 nm shift in peak position are evident.

The Z-average diameter of MNPs was measured as approximately 206 nm, whereas MNP-Fe^{3+}s exhibited a slightly larger size of 214.4 nm. The polydispersity index (PI) values for both structures were found to be 0.03265 and 0.03636, respectively, indicating that the nanoparticles have a homogeneous distribution and exhibit monodisperse characteristics. Additionally, the measurement reliability for MNP and MNP-Fe^{3+} structures was determined as 364.1 kcps and 359.3 kcps, respectively. Table 4.1 shows the particle size distribution obtained from DLS measurements.

Table 4.1
DLS measurements of MNPs and MNP-Fe^{3+}s.

Sample	Z-Average (nm)	Polydispersity Index (PDI)	Measurement Reliability (kcps)
MNP	206	0.03265	364.1
MNP-Fe^{3+}	214.4	0.03636	359.3

Correlation functions (g_2-1 vs. time) for MNPs (blue solid line) and MNP-Fe^{3+}s (red dashed line) are presented in Figure 4.2.

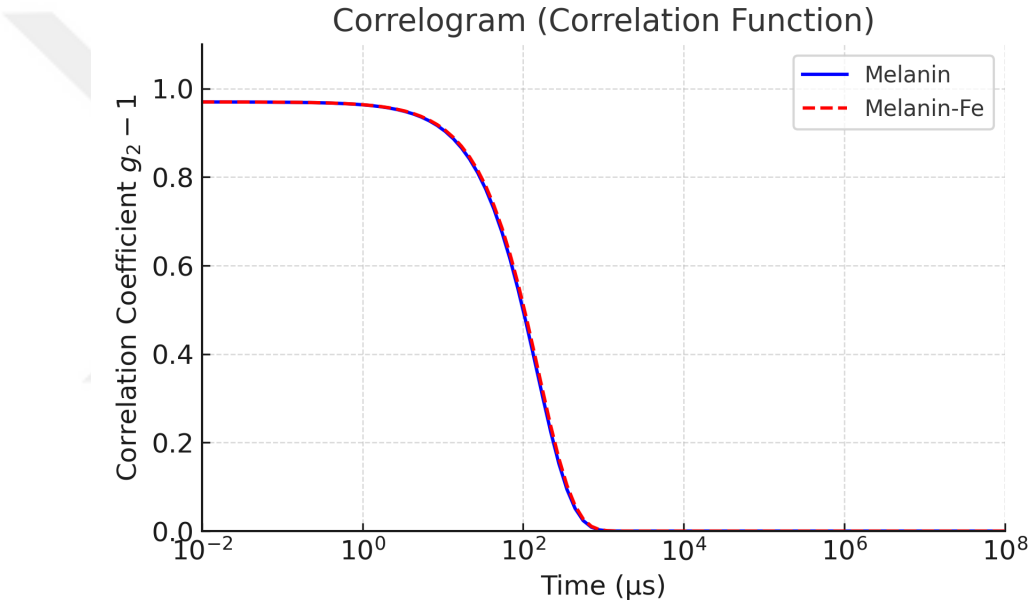

Figure 4.2 Size-intensity distribution comparison of MNPs and MNP-Fe^{3+}s.

Both correlograms start at a high initial correlation (0.97 at the shortest delay times) and decay to zero at long delay times, consistent with monodisperse particles. The MNP-Fe^{3+} samples correlation decays slightly more slowly (the red dashed curve lies just above the blue curve in the mid-decay region), reaching the baseline at a slightly longer delay time. This indicates a slightly lower diffusion coefficient, in line with its larger particle size. Axes are labeled as in the DLS instrument output: time in microseconds (log scale from 10^{-2} to 10^{8} μs) and the correlation coefficient (g_2-1) on the linear Y-axis. Both curves demonstrate the excellent data quality (smooth decay and high intercept) and the close similarity in dynamic size, with MNP-Fe^{3+}s displaying

a modest increase in hydrodynamic diameter as reflected by its slower decorrelation. The low fit error values (0.0004563 and 0.0005245) support the high accuracy of the measurements.

4.1.2 Functional Group Analysis by FTIR

The FTIR spectral analysis provided comparative insights into the functional groups present in both MNP and MNP-Fe^{3+} structures. The characteristic absorption bands observed in both samples are summarized in Table 4.2.

Table 4.2
Comparison of FTIR spectral bands of MNPs and MNP-Fe^{3+}s.

Peak Point (cm^{-1})	MNP	MNP-Fe^{3+}	Comment
3300-3400	O-H streching	Weakening, shifting	Interaction with iron, phenolic OH binding
1600-1700	C=O streching	Decrease in amplitude	Iron coordination, change in carbonyl structure
1400-1500	C-N/C=C aromatic	Increase in amplitude	Metal-amine interaction

The characteristic broad band observed in the 3300-3400 cm^{-1} region in MNPs is attributed to O-H or N-H stretching vibrations, which are indicative of phenolic OH or amine groups. The prominent peak within the 1600-1700 cm^{-1} region corresponds to C=O stretching, typically associated with quinone structures and carbonyl-containing aromatic rings. Additionally, the 1400-1500 cm^{-1} band indicates C-N stretching or C=C aromatic ring vibrations, representing indole structures or amide linkages. The absorption in the 1000-1200 cm^{-1} range, attributed to C-O-C stretching, signifies the presence of phenolic structures or polysaccharide content. As shown in Figure 4.3, the spectral profiles of MNP and MNP-Fe^{3+} exhibit notable differences primarily in the OH and C=O regions, highlighting the structural modifications induced by iron coordination.

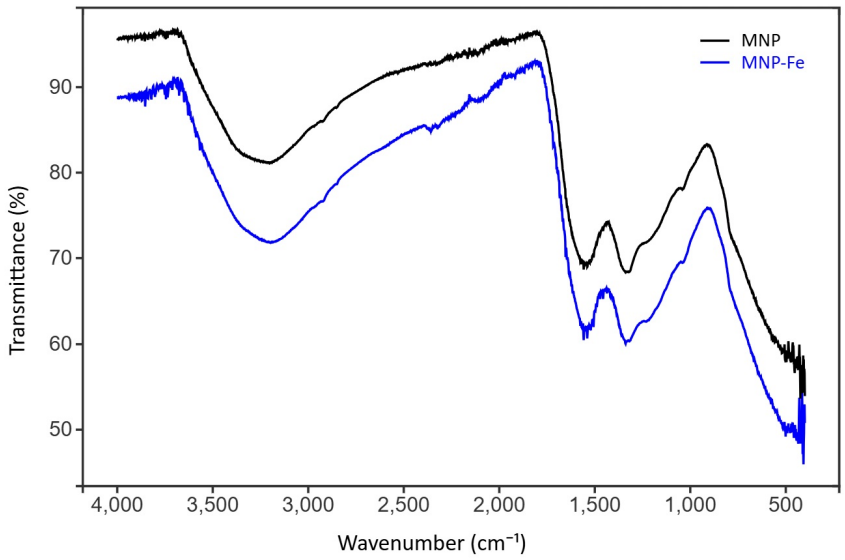

Figure 4.3 FTIR spectra of MNPs and MNP-Fe^{3+}s.

4.1.3 Optical Properties by UV-Vis Spectroscopy

The UV-Vis absorption spectra of MNPs and MNP-Fe^{3+}s is presented in Figure 4.4.

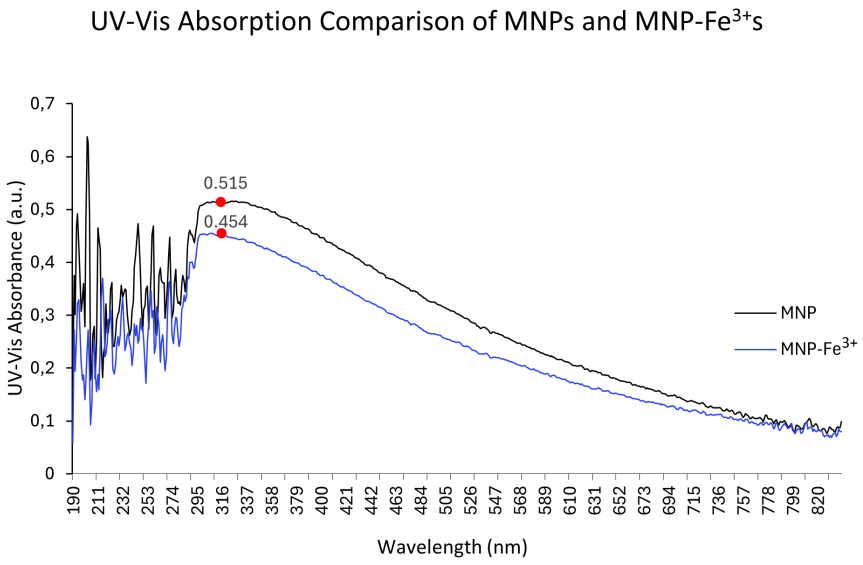

Figure 4.4 UV-Vis absorption comparison of MNP and MNP-Fe^{3+}s.

The spectra, encompassing both the visible and ultraviolet regions, were acquired across a wavelength range of 190 to 840 nm.

The UV-Vis spectra reveal that both MNPs and MNP-Fe^{3+}s exhibit a characteristic broad absorption band in the UV region, with the most prominent peak observed around 320 nm. The MNP spectrum shows a maximum absorbance of 0.515 at approximately 320 nm. The absorbance rises sharply from 190 nm, reaching a peak around 320 nm, followed by a gradual decline throughout the visible region. In contrast, the MNP-Fe^{3+} spectrum shows a slightly lower maximum absorbance of 0.454 at the same wavelength (320 nm). The increase in absorbance from 190 to 320 nm is more moderate compared to pure melanin, and the subsequent decline in the visible range is steeper.

The comparison of absorbance values between MNPs and MNP-Fe^{3+}s at the peak wavelength (320 nm) is detailed in Table 4.3.

Table 4.3
Absorbance characteristics of MNPs and MNP-Fe^{3+}s.

Feature	MNP	MNP-Fe^{3+}	Comment
Maximum Absorbance	0.515	0.454	Absorbance decrease after iron loading
Peak Wavelength (nm)	320	320	No shift in peak point, but there is an amplitude difference
Absorbance Curve	Steeper rise	Softer rise	Shows that iron reduces absorption capacity
Absorbance Decrease Rate (after 320)	Slow decrease	Fast decrease	Iron loading reduces the stable absorption in the UV region

4.1.4 Morphological Characterization by SEM

The morphological characteristics of MNPs and MNP-Fe^{3+}s were examined using Scanning Electron Microscopy (SEM). The primary objective was to evaluate

the structural differences between non-chelated MNPs and those modified through iron chelation, focusing on particle size, shape, surface morphology, and agglomeration tendencies.

SEM images of both MNPs and MNP-Fe^{3+}s reveal that the nanoparticles predominantly exhibit a spherical morphology, characterized by smooth and homogenous surfaces. The images clearly demonstrate that both types of nanoparticles maintain their spherical structure despite the incorporation of iron. However, there are some noticeable differences between the two types, particularly in terms of particle size and agglomeration.

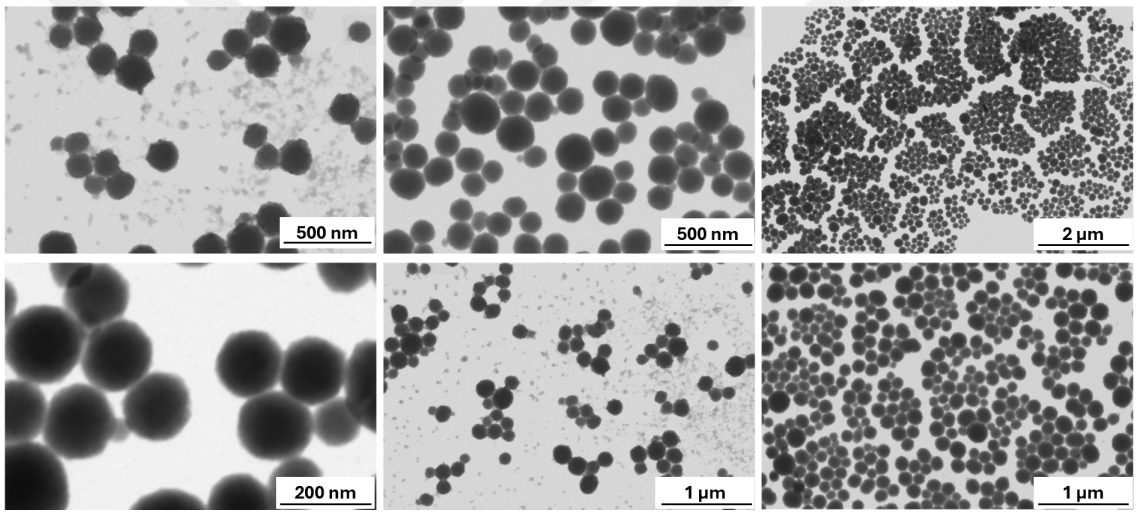

Figure 4.5 SEM images of MNPs.

As seen in Figure 4.5, MNPs indicate a relatively uniform size distribution, with particle diameters ranging between 100 nm and 200 nm with an average of 150 nm. The particles exhibit smooth surfaces with minimal roughness, and no significant structural anomalies were detected. Furthermore, the degree of agglomeration in MNP samples was relatively low, indicating good dispersion stability.

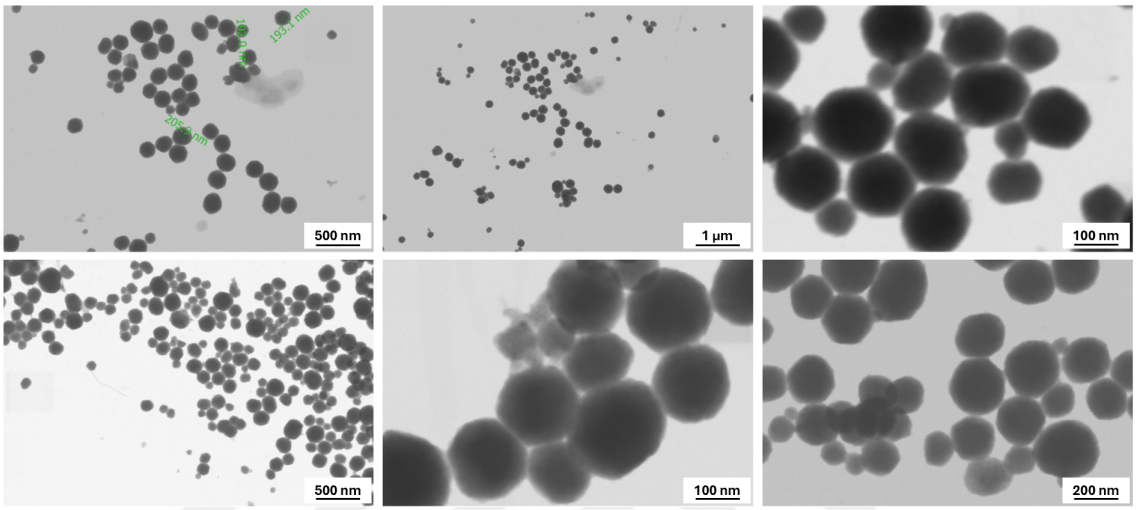

Figure 4.6 SEM images of MNP-Fe^{3+}s.

As seen in Figure 4.6, MNP-Fe^{3+}s display a slightly larger size distribution but no significant change in overall range and mean sizes was seen. This slight increase in size can be attributed to the chelation process, where the coordination of iron ions with melanin molecules may cause minor particle growth. The surfaces of MNP-Fe^{3+}s appear somewhat less smooth compared to non-chelated MNPs, potentially due to the incorporation of iron oxides or altered surface chemistry. Additionally, MNP-Fe^{3+} images reveal a more pronounced tendency for agglomeration, particularly in high-magnification images where small clusters are evident.

4.2 Simulation Results

In this study, simulations were performed to investigate the behavior of melanin MNPs and MNP-Fe^{3+}s in two distinct environments: water and blood. The primary objective was to evaluate the impact of iron chelation on the optical and thermal properties of MNPs under varying conditions.

To accurately model the interactions and behavior of nanoparticles, the simulations were conducted separately in both water and blood media. These environments were chosen to reflect the potential biological contexts where nanoparticles may be applied, such as biomedical therapies and diagnostic applications. The physical and optical properties of both media, including refractive index and thermal conductivity, were carefully defined to ensure realistic modeling. The parameters used for each environment are presented in methodology. Simulations were conducted by applying light source irradiation at 100 mW/cm^2 power density for 30 minutes in three distinctive wavelengths of 530 nm, 633 nm and 785 nm.

4.2.1 Heat Distribution Profiles in Simulations

The simulation results revealed notable differences in the behavior of MNP and MNP-Fe^{3+} when dispersed in water and blood. In water, both nanoparticle types exhibited similar absorption profiles, characterized by a pronounced peak around the target wavelength region. Heat distribution graph of MNP dispersed in water is presented in the Figure 4.7 after irridation with 530 nm light source is given as an example of the obtained heat distribution profile. The results obtained with other light sources (633 nm and 785 nm) and other media (blood) are collectively presented in Table 4.4.

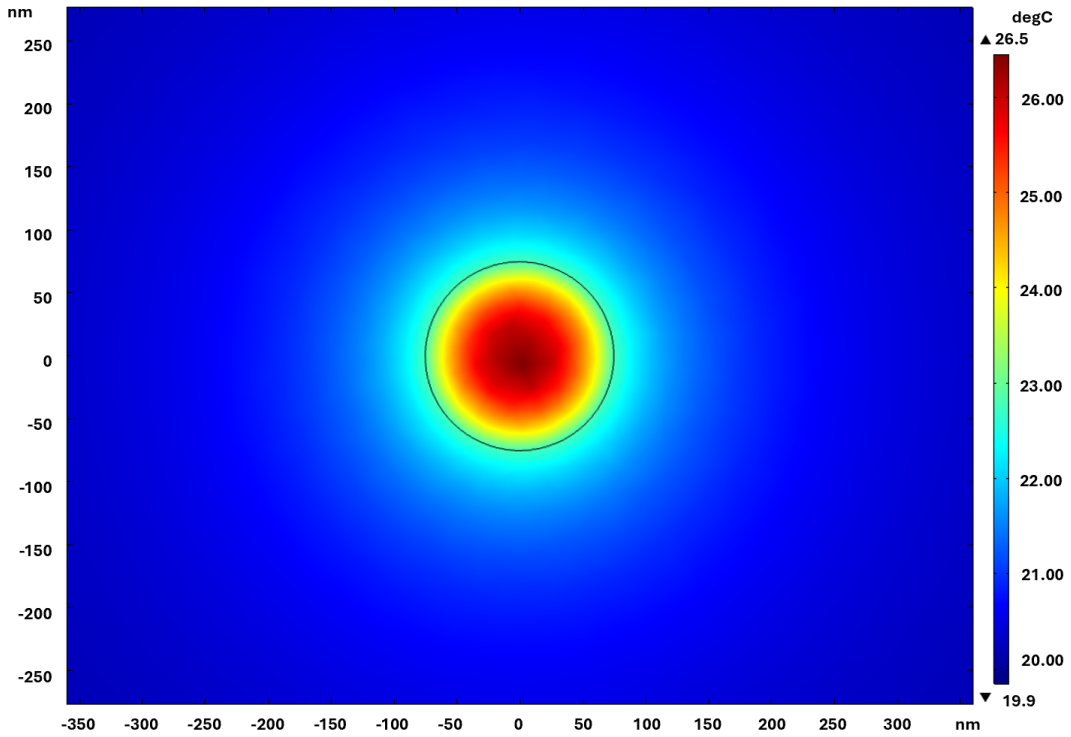

Figure 4.7 Heat distribution profile of MNP dispersed in water after simulation of 530 nm light source irridation.

However, the presence of iron in MNP-Fe^{3+} resulted in a slight shift in the peak position, indicating an alteration in optical properties due to chelation. Heat distribution graph of MNP-Fe^{3+} dispersed in distilled water after irridation with 530 nm light source is presented in the Figure 4.8.

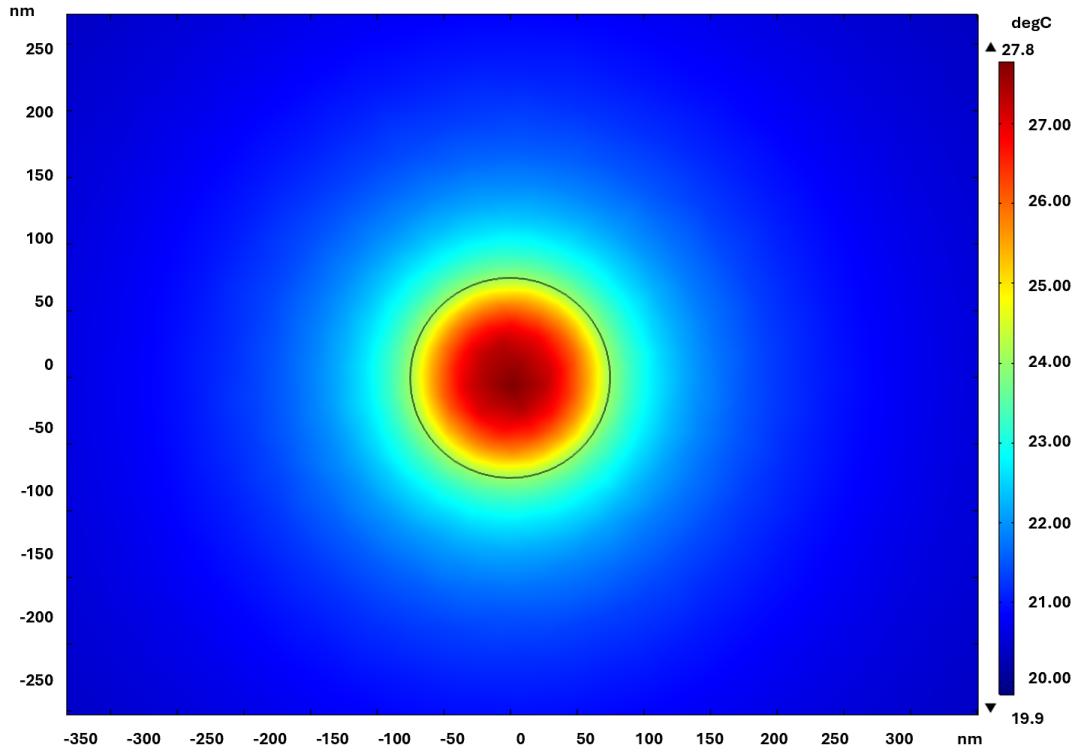

Figure 4.8 Heat distribution profile of MNP-Fe^{3+} dispersed in water after simulation of 530 nm light source irridation.

In contrast, complex composition and higher refractive index of blood led to a more pronounced shift in the absorption spectrum, particularly for MNP-Fe^{3+}. The temperature variations observed in the simulation studies, where light source irradiation was initiated at 20°C under different environmental conditions and wavelengths, are summarized in Table 4.4.

Table 4.4
Comparison of temperature changes after light source irridation simulations of MNP and MNP-Fe^{3+}.

WL (nm)	MNP in DW	MNP-Fe^{3+} in DW	MNP in Blood	MNP-Fe^{3+} in Blood
530	26.5°C	27.8°C	27.1°C	28.7°C
633	24.8°C	25.9°C	25.2°C	26.6°C
785	24.6°C	25.1°C	25.0°C	25.7°C

How nanoparticle size affects the temperature increase was also investigated and the findings for MNP and MNP-Fe^{3+} are presented in Table 4.5 and Table 4.6 individually.

Table 4.5
Comparison of simulated temperature changes of MNP with different sizes after light source irradiation.

Medium	Distilled Water			Blood		
LS WL / NP Radius (nm)	50	75	100	50	75	100
530	22.8°C	26.5°C	31.5°C	23.0°C	27.0°C	32.6°C
633	22.0°C	24.8°C	28.5°C	22.2°C	25.2°C	29.3°C
785	22.0°C	24.6°C	28.2°C	22.1°C	25.0°C	29.0°C

Table 4.6
Comparison of simulated temperature changes of MNP-Fe^{3+} with different sizes after light source irradiation.

Medium	Distilled Water			Blood		
LS WL / NP Radius (nm)	50	75	100	50	75	100
530	23.4°C	27.8°C	33.9°C	23.7°C	28.6°C	35.4°C
633	22.5°C	25.9°C	30.5°C	22.8°C	26.5°C	31.6°C
785	22.2°C	25.1°C	29°C	22.4°C	25.6°C	30°C

4.2.2 Surface Temperature Profiles

The presented simulation results in this section show the surface and isosurface temperature distributions for MNP and MNP-Fe^{3+} in both distilled water and blood environments. The surface temperature distribution obtained from the simulation for MNP under 530 nm laser irradiation in distilled water is presented in Figure 4.9. As observed, the localized temperature around the nanoparticle reached approximately 22.8°C. The values obtained here show the maximum temperature reached by the environment in which the nanoparticle is located, in this case the distilled water environment.

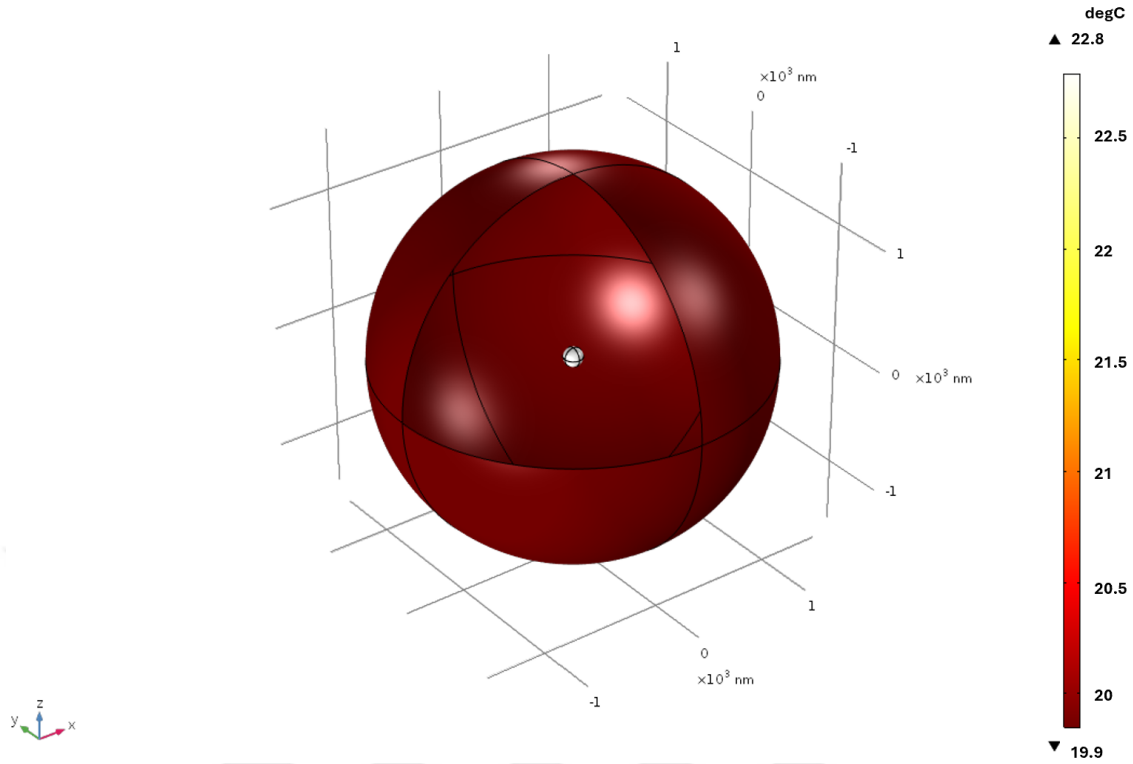

Figure 4.9 The surface temperature distribution obtained from the simulation for MNP under 530 nm laser irradiation in distilled water.

In contrast, Figure 4.10 presents the corresponding isosurface temperature distribution. The resulting isothermal volume provides a visual indication of the thermal penetration range into the surrounding medium. While the highest temperatures were concentrated near the nanoparticle surface, a significant thermal diffusion was observed within the medium, suggesting a potentially effective therapeutic radius for localized heating.

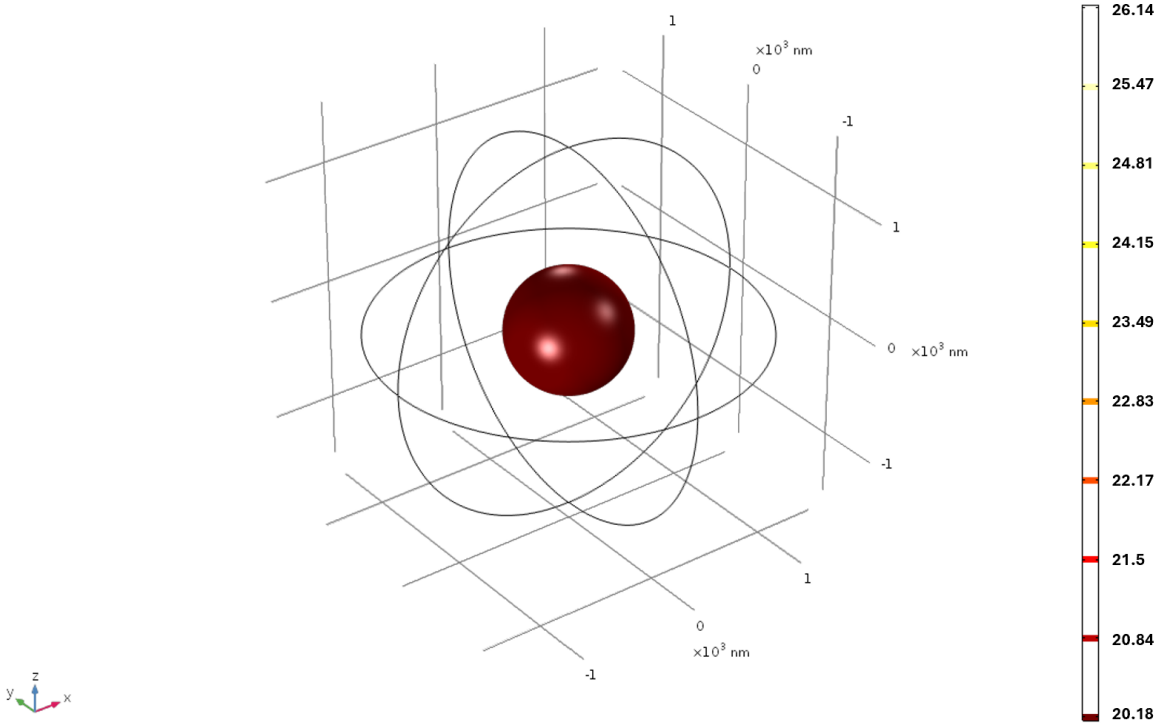

Figure 4.10 The isothermal surface temperature distribution obtained from the simulation for MNP under 530 nm laser irradiation in distilled water.

Similarly, Figure 4.11 shows the surface temperature distribution of MNP in blood medium. When comparing the two surrounding media, the temperature elevation in distilled water was generally lower than in blood, which can be attributed to the thermal conductivity and absorptive properties of biological tissues, resulting in the difference in heat dissipations.

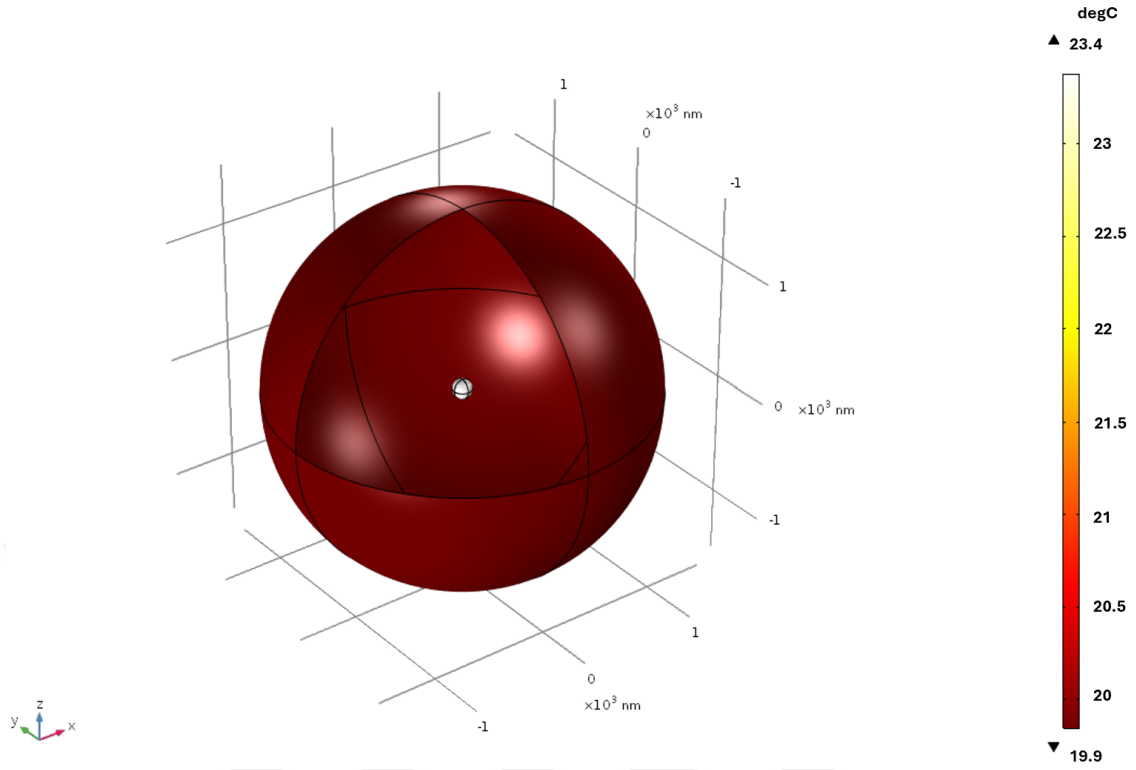

Figure 4.11 The surface temperature distribution obtained from the simulation for MNP under 530 nm laser irradiation in blood.

In addition to the representative figures shown in Figures 4.9, 4.10 and 4.11, a comprehensive set of simulations was conducted to evaluate the thermal behavior of both MNP and MNP-Fe^{3+} under laser irradiation at 530 nm, 633 nm, and 785 nm wavelengths in both distilled water and blood environments.

The simulations revealed that MNP-Fe^{3+} consistently exhibited higher surface temperatures compared to MNP across all laser wavelengths, likely due to enhanced optical absorption resulting from iron chelation. Moreover, laser wavelength had a significant impact, with 530 nm generally leading to higher photothermal conversion than 633 nm or 785 nm, especially in the blood environment.

4.2.3 Electric Field Profile

The electric field distribution around the MNP and MNP-Fe^{3+} was analyzed to evaluate their electromagnetic response under light source irradiation. The simulation was run multiple times for nanoparticles of different sizes. The simulation result image obtained with a 75 nm radius MNP under 530 nm light source irridiation is presented as an example in Figure 4.12.

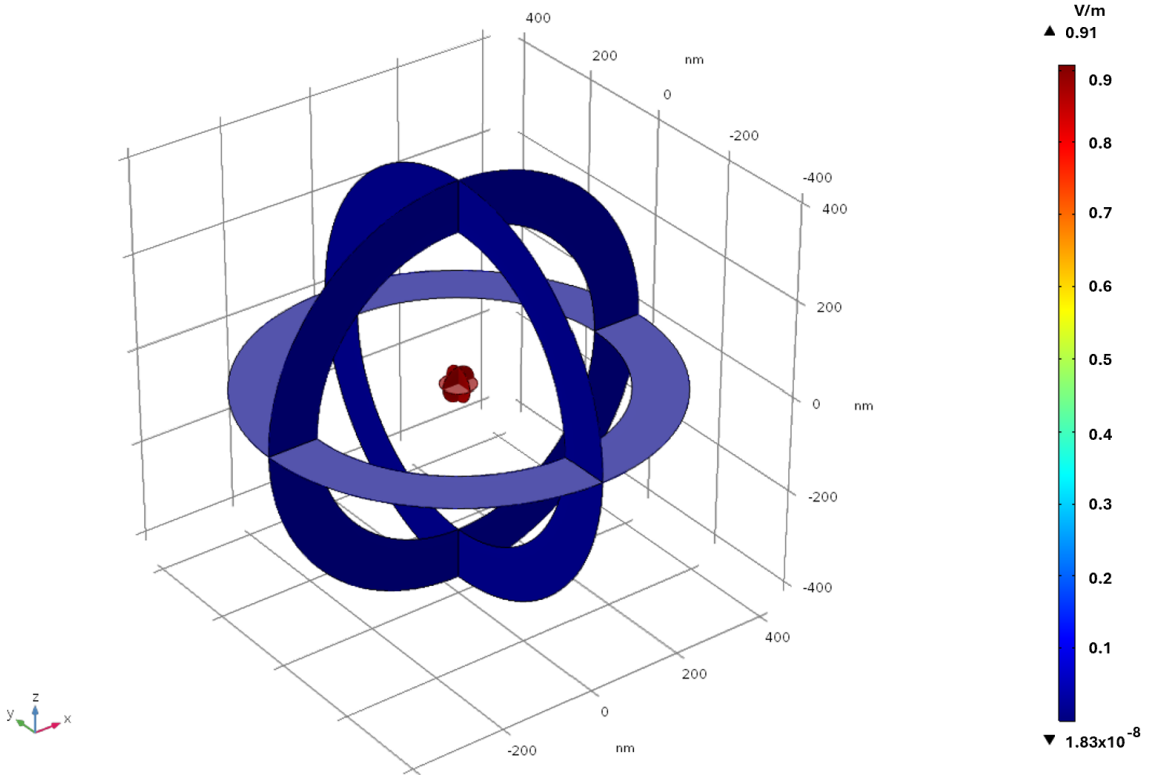

Figure 4.12 Electric field distribution of MNP under light source irradiation.

To comprehensively evaluate the optical properties and photothermal efficiency of both MNP and MNP-Fe^{3+}, simulations were conducted for particles of varying sizes. Specifically, the radii considered in the simulations for both MNP and MNP-Fe^{3+} were 50 nm, 62.5 nm, 75 nm, 87.5 nm, and 100 nm. The absorption cross-section (σ_{abs}) spectra of these nanoparticles were calculated for a range of wavelengths. Absorption cross section (σ_{abs}) spectra for MNP is presented in Figure 4.13.

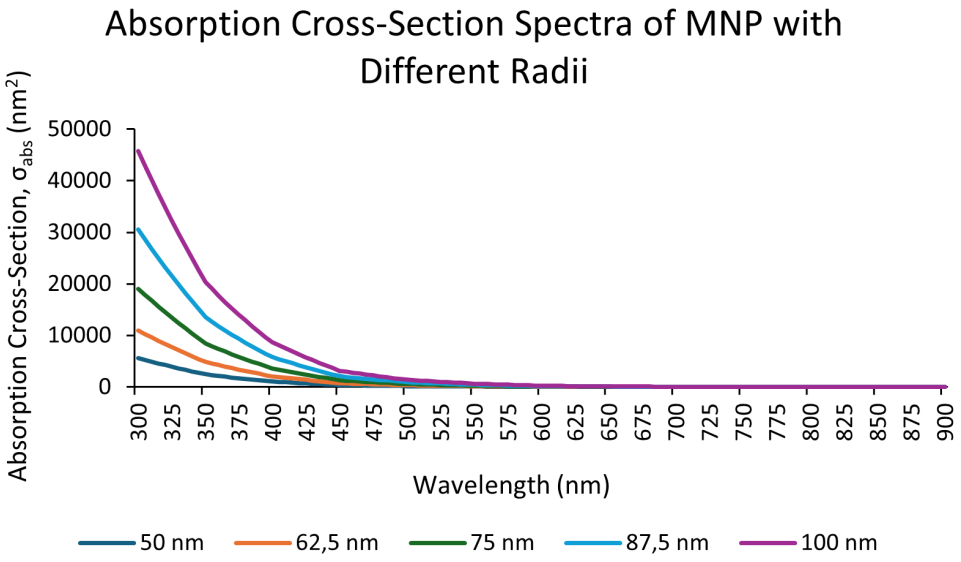

Figure 4.13 Absorption cross-section spectra of MNP with different radii.

Absorption cross section (σ_{abs}) spectra for MNP-Fe^{3+} is presented in Figure 4.14.

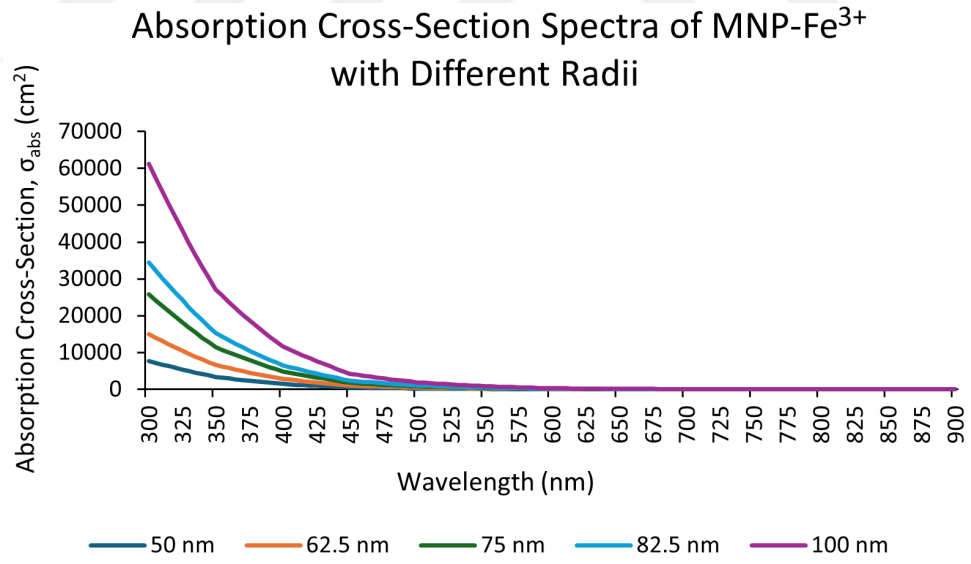

Figure 4.14 Absorption cross-section spectra of MNP-Fe^{3+} with different radii.

4.3 Experimental Results

4.3.1 Photothermal Heating Under Light Source Irradiation

This section evaluates the temperature variations observed when MNPs and MNP-Fe^{3+}s are exposed to different light source wavelengths of 530 nm, 633 nm, and 785 nm. The temperature measurements were taken at regular intervals, with each light source wavelength applied to both MNP and MNP-Fe^{3+} samples dispersed in distilled water. Baseline measurements were recorded prior to light source irradiation to establish initial temperature conditions for each sample. The initial temperature of all solutions and distilled water was 22.0°C. Additionally, control measurements in distilled water without nanoparticles were conducted to account for any inherent temperature changes unrelated to nanoparticle heating. The experimental results were systematically recorded and presented in Table 4.5.

Table 4.7
Highest temperatures recorded after light source irridation MNPs and MNP-Fe^{3+}s.

	530 nm	633 nm	785 nm
MNP	28.6°C	27°C	26.9°C
MNP-Fe^{3+}	29.5°C	27.5°C	27.1°C
Distilled Water	22.8°C	22.8°C	22.8°C

Graphical comparisons of temperatures obtained with light sources with different wavelengths is presented in the graphs below.

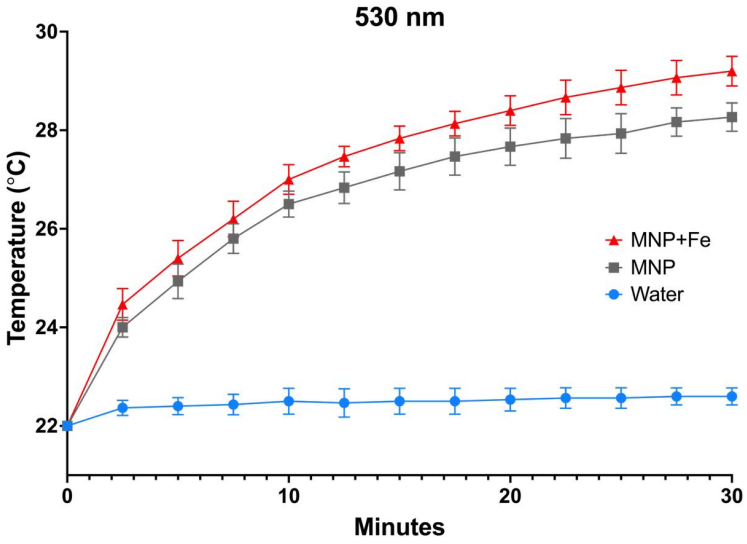

Figure 4.15 Comparison of the temperatures obtained with the 530 nm light source.

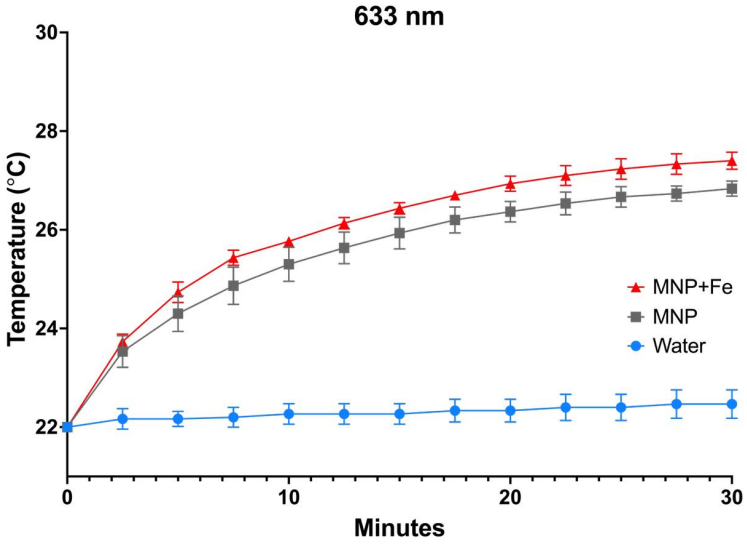

Figure 4.16 Comparison of the temperatures obtained with the 633 nm light source.

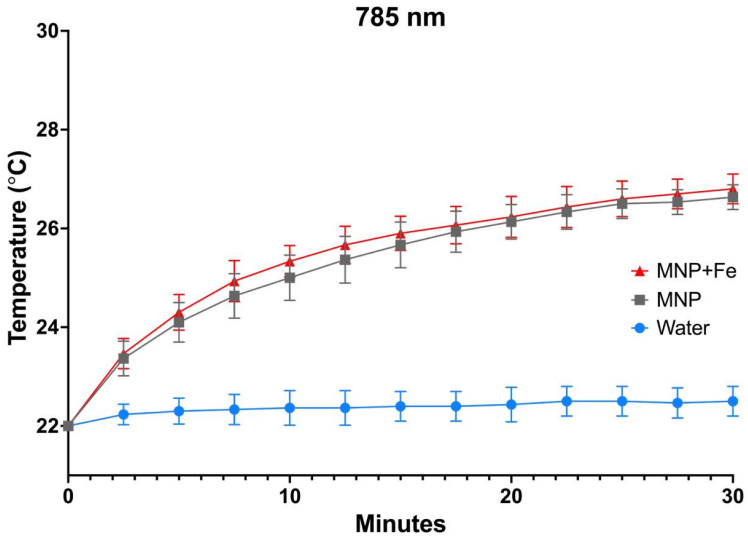

Figure 4.17 Comparison of the temperatures obtained with the 785 nm light source.

4.4 Comparison of Simulation and Experimental Results

A correlation analysis was performed between the simulated and experimental temperature data obtained for MNP, MNP-Fe^{3+}, and distilled water at three different wavelengths.

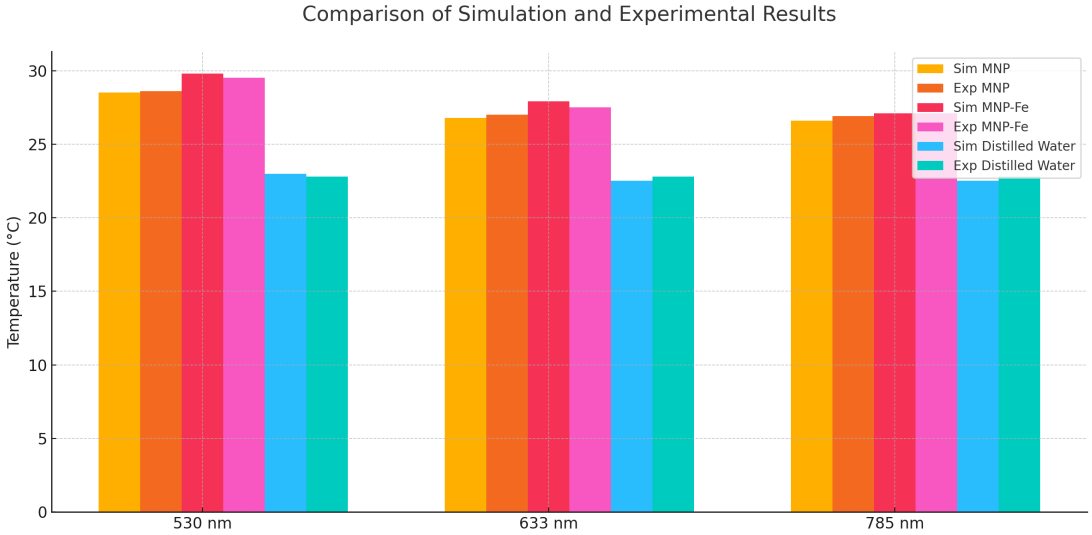

Figure 4.18 Comparison of simulation and experimental results.

The temperatures used in the correlation were extracted from 30-minute endpoint values under identical conditions. As shown in Figure 4.19, a strong linear relationship was observed between the experimental and simulated results, with a coefficient of determination (R^2) of 0.992. This high correlation confirms that the simulation model effectively predicts the photothermal behavior of the nanoparticles in distilled water and validates the accuracy of the computational approach.

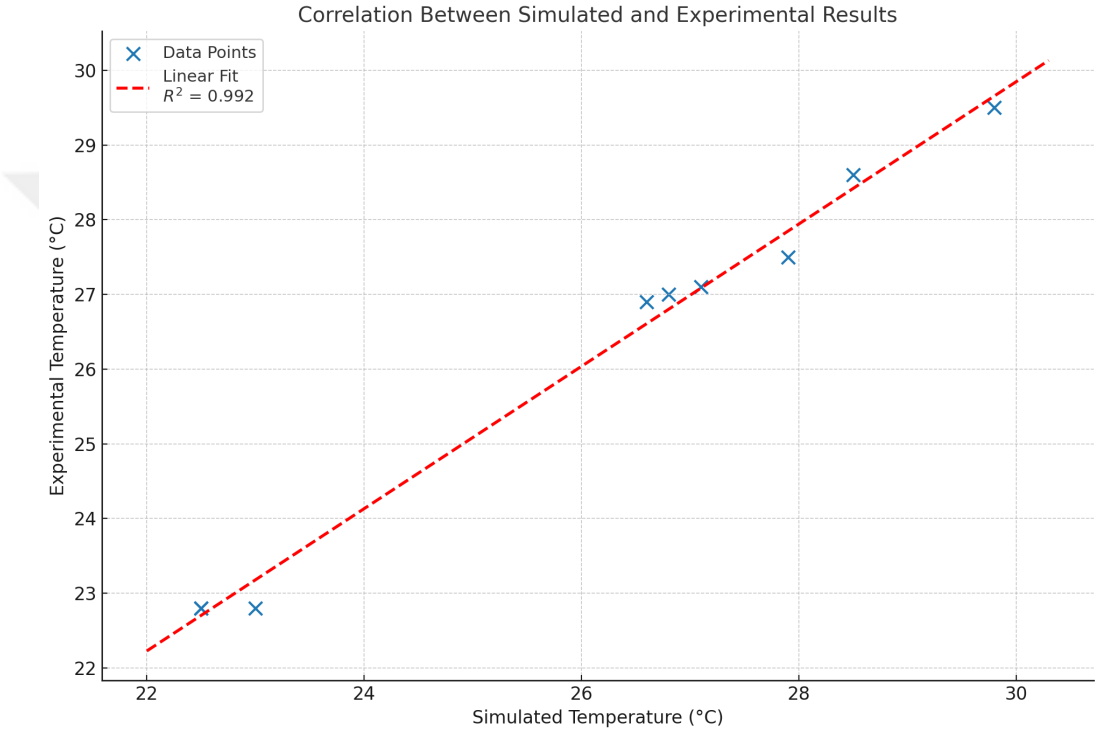

Figure 4.19 Correlation plot comparing the simulated and experimental temperature values.

4.5 Summary of Key Findings

In this study, the photothermal response of MNPs and MNP-Fe^{3+}s was systematically investigated through both experimental measurements and computational simulations. The results revealed that MNP-Fe^{3+}s exhibited superior photothermal conversion efficiency compared to MNPs when exposed to light source irradiation at wavelengths of 530 nm, 633 nm, and 785 nm. Experimental data demonstrated higher temperature increments for MNP-Fe^{3+}s, particularly under 530 nm light source expo-

sure, confirming the enhanced absorption and heat generation properties attributed to iron incorporation.

Simulations aligned with experimental trends, indicating that MNP-Fe^{3+} consistently achieved higher surface temperatures than MNP across all tested wavelengths. However, minor differences were observed between simulated and experimental temperatures, primarily due to differences in heat dissipation dynamics and light source intensity distribution between the idealized simulation environment and actual experimental conditions.

Overall, the comparative analysis highlights the potential of MNP-Fe^{3+} as an efficient photothermal agent, with the simulation models offering a reliable prediction framework for thermal behavior under light source irradiation. Future studies are recommended to optimize simulation parameters to better mirror experimental conditions, particularly considering nanoparticle aggregation and localized heating effects.

5. DISCUSSION

The primary objective of this study was to investigate the photothermal performance of melanin nanoparticles (MNPs) and iron-chelated melanin nanoparticles (MNP-Fe^{3+}s) of various sizes and under light source irradiation at various wavelengths. Both simulation and experimental approaches were used to comprehensively determine the temperature increase induced by light source exposure. The findings not only highlight the significant influence of nanoparticle composition, medium and the nanoparticle size on photothermal efficiency but also reveal critical insights into the interaction between light source parameters and nanoparticle characteristics.

The first step in the overall study was DLS, SEM, FTIR and UV-Vis absorbance analysis to determine the characteristic properties of nanoparticles.

DLS results indicated that the introduction of iron into the melanin structure results in a slight increase in particle size, although this increase is minimal and does not significantly alter the general morphology of the nanoparticles.

One of the critical observations from SEM analysis is the difference in agglomeration patterns between MNPs and MNP-Fe^{3+}s. The particle size distribution analysis based on the SEM images reveals that MNPs exhibit a relatively uniform and monodisperse morphology, with an average diameter of approximately 150 nm. MNP-Fe^{3+} samples have a slight incerase in nanoparticle size. With diameters ranging from 140 nm up to 200 nm, with an average of 170 nm. MNPs appear relatively well-dispersed, maintaining a profile with limited particle clustering. This characteristic is crucial for applications requiring stable nanoparticle suspensions, such as in biomedical or photothermal applications. On the other hand, MNP-Fe^{3+} samples exhibit a higher degree of particle clustering, which could be due to increased interparticle interactions following iron chelation. The presence of iron within the nanoparticle matrix may increase surface charge variations, leading to enhanced particle-particle attraction. The

formation of small aggregates is particularly prominent in samples with higher magnification, suggesting that the iron coordination might alter the surface characteristics, promoting agglomeration. The increased agglomeration may affect the optical properties and photothermal efficiency of MNP-Fe^{3+}s, highlighting the need for surface modification or stabilization techniques to maintain dispersion quality. Similar findings were reported in the study by Tian et al., where melanin-based nanoparticles chelated with metal ions exhibited higher aggregation tendencies due to altered surface charge distributions. This aggregation behavior, while potentially enhancing magnetic or photothermal properties, was also noted to compromise colloidal stability. Therefore, the observed clustering in MNP-Fe^{3+}s in this study aligns with prior findings and underlines the importance of controlling interparticle interactions when designing Fe^{3+}-chelated MNPs for biomedical applications [26].

In the FTIR spectrum of MNP-Fe^{3+}s, a noticeable shift and a reduction in the intensity of the O-H stretching band were observed, indicating possible interactions between iron ions and phenolic OH groups. Similarly, the decreased intensity in the carbonyl stretching region (1600-1700 cm^{-1}) suggests that iron may coordinate with carbonyl groups within the MNP structure. In contrast, the aromatic C-H bending regions (600-800 cm^{-1}) exhibited no significant changes, suggesting that the core aromatic structure of MNPs remains preserved upon iron loading. These findings are in agreement with the study conducted by Chen et al., which demonstrated that the chelation of metal ions, particularly Fe^{3+}, to endogenous MNPs results in notable shifts in FTIR absorption bands associated with hydroxyl and carbonyl groups, confirming the coordination between iron and melanin functional moieties [35].

However, according to Solano et al., the way that metal ions bind to melanin can vary greatly depending on the melanin polymer's structural arrangement, oxidation state, and environmental factors. In some cases, this can lead to minimal or unclear FTIR spectral shifts because of overlapping vibrational modes or low binding efficiency [16]. Thus, even though the iron coordination theory is supported by the spectrum alterations seen in this investigation, other possibilities such weak, non-specific contacts or partial oxidation of functional groups cannot be completely ruled out.

The UV-Vis spectra revealed that both MNPs and MNP-Fe^{3+}s exhibit a characteristic broad absorption band in the UV region, with the most prominent peak observed around 320 nm. This peak corresponds to the strong light absorption property of melanin due to its inherent aromatic and conjugated structure. The MNP spectrum shows a maximum absorbance of 0.515 at approximately 320 nm. The absorbance rises sharply from 190 nm, reaching a peak around 320 nm, followed by a gradual decline throughout the visible region. This gradual decrease indicates that MNPs have a broad light absorption capacity, particularly in the UV range. In contrast, the MNP-Fe^{3+} spectrum shows a slightly lower maximum absorbance of 0.454 at the same wavelength (320 nm) although exhibiting larger temperature increases under laser irradiation. Given that higher absorbance usually corresponds with greater photothermal conversion, this may initially appear contradictory. The partial aggregation or incomplete dispersion of MNP-Fe^{3+} particles in solution, however, limits their optical path contribution during UV-Vis studies, which explains the reduced absorbance. Because of improved thermal conductivity, changed electronic structure, or increased photothermal conversion efficiency linked to Fe^{3+} chelation, MNP-Fe^{3+} may still have superior photothermal performance even with the lower observed absorbance. These findings emphasize how crucial it is to take into account both optical and physicochemical characteristics when assessing a nanomaterial's photothermal behavior. Similar findings were reported by Tian et al., where metal-chelated melanin structures showed altered dispersion behavior, affecting their spectral profile [26].

On the other hand, according to Silvestri et al., a steady relationship between absorbance and photothermal performance is generally anticipated, and variations from this pattern might be the result of experimental errors or restrictions in the conditions used for measurement rather than actual variations in nanoparticle efficiency [28]. In the study it was indicated that study turbidity in solution and heterogeneous particle distribution can cause UV-Vis spectroscopy to underestimate true absorbance levels. This viewpoint emphasizes how crucial it is to supplement spectrum studies with other techniques, such DLS or microscopy, in order to validate the dispersion state of nanoparticles and guarantee precise interpretation of absorbance-based photothermal evaluations.

The temperature increase of MNPs and MNP-Fe^{3+}s under light source irradiation was investigated through both experimental measurements and computational simulations. The comparison of results aims to evaluate the thermal response accuracy predicted by the simulation models when subjected to different light source wavelengths of 530 nm, 633 nm, and 785 nm in distilled water as the medium.

The temperature measurements that were obtained with the simulations indicated that the photothermal response of both MNP and MNP-Fe^{3+} varies significantly with wavelength and nanoparticle composition. In distilled water, the maximum temperature increase for MNP was observed at 530 nm, reaching 26.5°C, while the temperature at 633 nm and 785 nm remained relatively similar, at 24.8°C and 24.6°C, respectively. This suggests that the absorption efficiency of MNP is highest at 530 nm, which aligns with the absorption characteristics of melanin, known for its strong absorbance in the visible spectrum. In contrast, MNP-Fe^{3+}s exhibited a significantly enhanced photothermal response compared to MNPs, particularly at 530 nm, where the temperature rose to 27.8°C. At 633 nm and 785 nm, the temperature increases were measured as 25.9°C and 25.1°C, respectively. Among the wavelengths tested, the 530 nm light source resulted in the most substantial temperature increase for both MNP and MNP-Fe^{3+} samples, while the 785 nm light source produced the least heating effect. This wavelength dependence aligns with the absorption spectra of the nanoparticles, where shorter wavelengths correspond to higher absorption cross-sections. Similar findings were reported by Yang et al., who demonstrated that synthetic melanin nanoparticles exhibit wavelength-dependent photothermal conversion efficiency, with greater heating observed at shorter wavelengths due to higher optical absorption [21].

The photothermal performance of the nanoparticle's in blood exhibited a similar trend, with both MNPs and MNP-Fe^{3+}s achieving higher temperatures at 530 nm compared to longer wavelengths. For MNPs, the temperature increased to 27.0°C at 530 nm, while it was recorded as 25.2°C at 633 nm and 25.0°C at 785 nm. These values suggest that blood, which inherently absorbs more in the red and near-infrared regions, slightly increases the photothermal efficiency compared to distilled water. In the case of MNP-Fe^{3+}, the temperature increases were notably higher, particularly at 530 nm,

where the temperature reached 28.6°C, indicating superior photothermal conversion. At 633 nm and 785 nm, the temperatures rose to 26.5°C and 25.6°C, respectively. The increased temperature for MNP-Fe^{3+} in blood compared to distilled water suggests that the iron chelation not only enhances absorption at visible wavelengths but also contributes to improved stability and reduced heat dissipation when interacting with blood components. This observation aligns with the findings of Li et al., who demonstrated that natural melanin nanoparticles exhibit enhanced photothermal efficacy in complex biological environments such as blood due to their intrinsic biocompatibility and high photothermal conversion efficiency [30].

The presented data indicated that MNP-Fe^{3+} consistently outperform non-chelated MNP in both distilled water and blood, regardless of the light source wavelength. The most significant enhancement is observed at 530 nm, where MNP-Fe^{3+} in blood reaches 28.6°C, compared to 27.0°C for non-chelated MNP. It should be noted that the temperature measurements in the simulation started from 20 degrees and there was a temperature increase of almost 9 degrees with MNP-Fe^{3+} and 7 degrees with MNP. This enhanced performance can be ascribed to the synergistic effect of iron incorporation, which may increase the nanoparticle's overall light absorption and heat conversion efficiency. Similar findings were reported by Liu et al., who demonstrated that natural melanin-based nanoparticles exhibited significantly improved photothermal properties when combined with metallic ions, thereby supporting their potential for enhanced photothermal cancer therapy applications [31].

Moreover, the relatively consistent temperature increases across both media suggest that the iron chelation process does not compromise the biocompatibility or dispersibility of MNP-Fe^{3+} in biological fluids. This stability is crucial for biomedical applications, such as photothermal therapy, where consistent and predictable temperature elevation is essential for therapeutic efficacy.

However, other researchers have reported that metal coordination, particularly with iron ions, can sometimes induce increased aggregation or precipitation in complex biological environments, potentially limiting long-term stability and bioavailability. For

example, Mahdavi et al. emphasized that iron oxide nanoparticle formulations require surface modifications to prevent clustering in serum-like conditions [27]. This suggests that while MNP-Fe^{3+}s may initially appear stable, additional surface engineering, such as polymer coatings or functional ligands, might be necessary to ensure prolonged dispersibility and therapeutic effectiveness in physiological media.

The simulation was also conducted separately for nanoparticles of different sizes. The results demonstrated that bigger particles exhibit higher absorption cross-sections, particularly at shorter wavelengths. However, excessively large particles might lead to aggregation and reduce the surface area available for interaction, which can counteract the benefits of increased size. These findings highlight the importance of particle size optimization in applications involving photothermal therapy. Similar observations were reported by Yang et al., who demonstrated that tailoring the size of synthetic MNPs significantly improved their photothermal conversion efficiency and therapeutic performance [21].

Moreover, it was observed that MNP-Fe^{3+} generally exhibited higher absorption cross-sections compared to MNPs of the same size, highlighting the significant influence of iron chelation on the optical properties of the nanoparticles. This enhancement can be attributed to the increased electronic interactions and localized surface plasmon-like effects introduced by iron ions, which augment the photothermal conversion efficiency. A comparable trend was noted by Chen et al., who reported that the presence of metal ions, including Fe^{3+}, modulates the optical and magnetic characteristics of melanin-based nanoparticles, thereby improving their performance in biomedical applications [35].

Consistently higher temperature increase observed in MNP-Fe^{3+} compared to MNPs, as how it was observed with the simulations. The maximum temperatures recorded for MNP-Fe^{3+}s were 29.5°C (530 nm), 27.5°C (633 nm), and 27.1°C (785 nm), while for MNPs, the corresponding temperatures were 28.6°C, 27°C, and 26.9°C, respectively. Both the simulation and experimental data revealed that MNP-Fe^{3+}s achieved superior heating effects, particularly at shorter wavelengths such as 530 nm.

This phenomenon can be attributed to the enhanced optical absorption properties imparted by the iron ions, which increase the overall absorption cross-section. Additionally, the incorporation of iron enhances the thermal conductivity of the nanoparticles, allowing for more effective heat dissipation and thereby sustaining higher temperatures. This characteristic makes MNP-Fe^{3+}s particularly suitable for applications requiring efficient heat generation, such as photothermal therapy.

The experimental results demonstrated a peak temperature of 29.5°C for MNP-Fe^{3+}s under 530 nm light source irradiation, compared to 28.6°C for MNPs. Simulations mirrored this trend, with the simulated temperatures slightly lower than the experimental values. This discrepancy may stem from factors such as environmental heat loss in the experimental setup, which is inherently absent in the idealized simulation conditions. The simulated temperature values, however, were slightly lower than the experimental data. However, while the initial temperature in the experimental study was 22.0°C, this value was 20.0°C in the simulation. In other words, the temperature increase amounts are close and support each other. As expected, the control sample (distilled water without nanoparticles) maintained a relatively stable temperature around maximum 22.8°C, indicating minimal light source absorption. These findings align with previous reports, such as those by Yang et al., who highlighted that metal ion-doped melanin nanoparticles can be tailored for enhanced photothermal efficiency due to improved light-to-heat conversion capabilities [21].

Nevertheless, alternative studies have reported that iron coordination may also lead to altered energy dissipation pathways, potentially affecting uniform heat generation. For instance, Silvestri et al. highlighted that particle aggregation and uneven energy distribution may compromise photothermal uniformity in metal-doped nanostructures, particularly when surface engineering is insufficient [28]. This implies that while MNP-Fe^{3+}s show promise in controlled laboratory settings, further optimization might be necessary to ensure consistent clinical outcomes.

The wavelength-dependent heating behavior observed in both nanoparticle types is closely related to the absorption cross-section spectra. In particular, the absorption

cross-section (σ_{abs}) of both MNPs and MNP-Fe^{3+}s significantly decreases as the wavelength increases from 530 nm to 785 nm. This behavior is consistent with the decline in temperature rise observed experimentally and predicted through simulations. The shorter wavelength (530 nm) effectively induces greater photothermal heating due to its higher absorption efficiency, while the longer wavelengths (785 nm) result in comparatively lower temperature increases. Similarly, Cuzzubbo et al. emphasized that wavelength selection critically influences the photothermal efficiency of melanin-like nanoparticles, particularly in biomedical applications targeting localized heating [43].

The heating efficiency of nanoparticles also demonstrated a dependency on the medium in which they were dispersed. Both distilled water and blood were utilized as dispersion media in simulations to evaluate the effect of biological environments on heating performance. The results consistently indicated that blood, as a complex biological medium, exhibited a slightly higher baseline temperature than distilled water. This phenomenon may be attributed to the inherent absorption properties of blood, particularly in the near-infrared region. Additionally, blood's higher viscosity and thermal conductivity compared to distilled water can facilitate localized heat retention, contributing to a slightly higher temperature rise. This observation aligns with previous studies done by Li et al. and Liu et al., indicating that the optical and thermal properties of biological fluids, such as blood, can significantly influence the photothermal performance of nanoparticles. The enhanced heat retention in blood is particularly relevant for in vivo applications, where the medium's properties can modulate nanoparticle behavior and treatment efficacy [30, 31].

The strong agreement between simulated and experimental temperature values reinforces the reliability of the computational model used in this study. Although minor differences were observed, likely due to experimental conditions such as heat loss to the environment or slight differences in nanoparticle dispersion, the overall correlation indicates that the model sufficiently captures the essential photothermal dynamics. This supports the use of simulation-based approaches in nanoparticle-based photothermal therapy design. The observed minor differences between experimental and simulation data can be attributed to several factors. One plausible explanation is the differ-

ence in heat dissipation between the theoretical model and the actual experimental conditions. In simulations, idealized boundary conditions and assumptions regarding homogeneous distribution and thermal conductivity of nanoparticles might have led to an underestimation of the actual heating efficiency. Additionally, the aggregation state of nanoparticles in the experimental setup may have resulted in localized heating, which is not fully replicated in the single-particle simulation model.

Another critical factor could be the variations in light source intensity distribution and absorption coefficient that are not entirely captured in the simulation. Experimentally, light source scattering within the colloidal suspension may enhance localized heating, while simulations often assume a uniform irradiation profile.

Although simulations provided valuable insights into the thermal behavior of nanoparticles, some limitations remain. The primary challenge lies in accurately replicating the dynamic environment of biological media. Factors such as protein corona formation, aggregation, and complex interactions with blood components were not fully captured in the simulation models. Furthermore, the spatial heterogeneity of temperature distribution, particularly within clustered nanoparticle assemblies, requires more advanced modeling approaches.

The current simulation was performed using a single nanoparticle model. For a more realistic representation, future studies aim to integrate more complex models that account for real-time aggregation behavior and heterogeneous heating, ideally designed based on SEM image analyses to accurately reflect their spatial distribution and interactions. Additionally, experimental validations with varying light source power densities and prolonged irradiation times would help to further establish the applicability of MNP-Fe^{3+}s in biomedical applications. Optimizing the iron-to-melanin ratio may also reveal further improvements in thermal conversion efficiency.

6. CONCLUSION

This study investigated the photothermal properties of melanin nanoparticles (MNPs) and iron-chelated melanin nanoparticles (MNP-Fe^{3+}s) through simulations and experimental analysis. The primary goal was to compare the temperature rise induced by light source irradiation at different wavelengths in different media to optimize the photothermal performance for biomedical applications.

Both simulation and experimental results consistently showed that MNP-Fe^{3+}s exhibits superior photothermal efficiency compared to MNPs. The highest temperature rise observed experimentally was 29.5°C for MNP-Fe^{3+}s under 530 nm irradiation, compared to 28.6°C for MNPs. Simulations supported this trend, although they predicted slightly lower temperatures, likely due to idealized conditions. The results also revealed that shorter wavelengths produced more significant temperature increases, consistent with the higher absorption cross-section at these wavelengths. Additionally, blood as a medium led to slightly higher temperature rises compared to distilled water, attributed to its optical and thermal properties.

Electric field distribution analysis indicated that MNP-Fe^{3+} generated more localized hotspots compared to MNP, consistent with enhanced photothermal effects. Moreover, the size-dependent study revealed that larger nanoparticles (100 nm) exhibited higher absorption cross-sections, although the tendency for aggregation suggests an optimal size range should be considered.

The study highlights the importance of iron incorporation for improved photothermal performance, optimal light source wavelength selection for maximum heating, and careful consideration of particle size to balance efficiency and stability. These findings contribute to the development of more efficient melanin-based nanoparticles for photothermal therapy, emphasizing the need for further studies to assess biological interactions and long-term stability in clinical applications.

REFERENCES

1. Baykara, O., "Kanser tedavisinde güncel yaklaşımlar," *Balıkesir Sağlık Bilimleri Dergisi*, Vol. 5, no. 3, pp. 154–165, 2016.
2. Cooper, G. M., and K. Adams, "The Cell: A Molecular Approach," Oxford University Press, 2022.
3. Lodish, H. F., "Molecular Cell Biology," Macmillan, 2008.
4. Baba, A. I., and C. Câtoi, "Comparative Oncology," 2010.
5. dos Santos Guimarães, I., R. D. Daltoé, A. L. Herlinger, K. P. Madeira, et al., "Conventional cancer treatment," *Cancer Treatment-Conventional and Innovative Approaches*, 2013.
6. Chu, E., "Cancer Chemotherapy," New York, NY: McGraw-Hill Education, 2017.
7. Ahmad, S. S., S. Duke, R. Jena, M. V. Williams, and N. G. Burnet, "Advances in radiotherapy," *BMJ*, Vol. 345, 2012.
8. Wyld, L., R. A. Audisio, and G. J. Poston, "The evolution of cancer surgery and future perspectives," *Nature Reviews Clinical Oncology*, Vol. 12, no. 2, pp. 115–124, 2015.
9. Zou, L., H. Wang, B. He, L. Zeng, *et al.*, "Current approaches of photothermal therapy in treating cancer metastasis with nanotherapeutics," *Theranostics*, Vol. 6, no. 6, p. 762, 2016.
10. Jaque, Da, Martínez M. L., del Rosal, B., Haro-Gonzalez, P., Benayas, A., et al., "Nanoparticles for photothermal therapies," *Nanoscale*, Vol. 6, no. 16, pp. 9494–9530, 2014.
11. Chen, J., C. Ning, Z. Zhou, P. Yu, et al., "Nanomaterials as photothermal therapeutic agents," *Progress in Materials Science*, Vol. 99, pp. 1–26, 2019.
12. Maeda, H., Wu, J., Sawa, T., Matsumura, Y., et al., "Tumor vascular permeability and the EPR effect in macromolecular therapeutics: a review," *Journal of Controlled Release*, Vol. 65, no. 1-2, pp. 271–284, 2000.
13. Peer, D., Karp, J. M., Hong, S., Farokhzad, et al., "Nanocarriers as an emerging platform for cancer therapy," *Nano-Enabled Medical Applications*, pp. 61–91, 2020.
14. Liu, H., Yang, Y., Liu, Y., Pan, J., et al., "Melanin-like nanomaterials for advanced biomedical applications: a versatile platform with extraordinary promise," *Advanced Science*, Vol. 7, no. 7, p. 1903129, 2020.
15. Wang, X., J. Sheng, and M. Yang, "Melanin-based nanoparticles in biomedical applications: From molecular imaging to treatment of diseases," *Chinese Chemical Letters*, Vol. 30, no. 3, pp. 533–540, 2019.
16. Solano, F., "Melanins: skin pigments and much moreâtypes, structural models, biological functions, and formation routes," *New Journal of Science*, Vol. 2014, no. 1, p. 498276, 2014.

17. Thody, A. J., E. M. Higgins, K. Wakamatsu, S. Ito, et al., "Pheomelanin as well as eumelanin is present in human epidermis," *Journal of Investigative Dermatology*, Vol. 97, no. 2, pp. 340–344, 1991.

18. Blázquez-Castro, A., and J. C. Stockert, "Biomedical overview of melanin. 1. updating melanin biology and chemistry, physico-chemical properties, melanoma tumors, and photothermal therapy," *Biocell*, Vol. 45, no. 4, p. 849, 2021.

19. Bayrak, E., P. Yiğit, E. Bakay, B. Sirek, et al., "Accelerating wound healing with combinatorial therapy using natural melanin nanoparticle-polyvinyl alcohol blend and core-sheath hybrid nanofibers under uv-a irradiation," *Macromolecular Materials and Engineering*, Vol. 309, no. 5, p. 2300382, 2024.

20. Eom, T., J. Jeon, S. Lee, K. Woo, et al., "Naturally derived melanin nanoparticle composites with high electrical conductivity and biodegradability," *Particle & Particle Systems Characterization*, Vol. 36, no. 10, p. 1900166, 2019.

21. Yang, P., S. Zhang, N. Zhang, Y. Wang, et al., "Tailoring synthetic melanin nanoparticles for enhanced photothermal therapy," *ACS Applied Materials & Interfaces*, Vol. 11, no. 45, pp. 42671–42679, 2019.

22. Solano, F., "Melanin and melanin-related polymers as materials with biomedical and biotechnological applications-cuttlefish ink and mussel foot proteins as inspired biomolecules," *International Journal of Molecular Sciences*, Vol. 18, no. 7, p. 1561, 2017.

23. Akman, B., B. İslam, G. K. Can, N. T. Avşar, et al., "Gıda ve sağlık uygulamaları için uv-a işıma altında alternatif bir fotokatalizör olarak: Doğal melanin nanoparçacıkları," *Avrupa Bilim ve Teknoloji Dergisi*, no. 32, pp. 940–946, 2021.

24. Kabay, G., A. E. Meydan, T. Eom, B. S. Shim, et al., "Stimuli-responsive nanoparticle-nanofiber hybrids for drug delivery and photodynamic therapy," *International Journal of Pharmaceutics*, Vol. 630, p. 122442, 2023.

25. Kaleli-Can, G., B. Ozlu, H. F. Özgüzar, B. Onal-Ulusoy, et al., "Natural melanin nanoparticle-decorated screen-printed carbon electrode: Performance test for amperometric determination of hexavalent chromium as model trace," *Electroanalysis*, Vol. 32, no. 8, pp. 1696–1706, 2020.

26. Tian, L., Li, X., Ji, H., Yu, Q., et al., "Melanin-like nanoparticles: advances in surface modification and tumour photothermal therapy," *Journal of Nanobiotechnology*, Vol. 20, no. 1, p. 485, 2022.

27. Mahdavi, M., M. B. Ahmad, M. J. Haron, F. Namvar, et al., "Synthesis, surface modification and characterisation of biocompatible magnetic iron oxide nanoparticles for biomedical applications," *Molecules*, Vol. 18, no. 7, pp. 7533–7548, 2013.

28. Silvestri, B., P. Armanetti, G. Pota, G. Vitiello, et al., "Enhanced Photoacoustic Response by Synergistic Ag–Melanin Interplay at the Core of Ternary Biocompatible Hybrid Silica-Based Nanoparticles," *ACS Applied Materials & Interfaces*, Vol. 15, no. 40, pp. 46756–46764, 2023.

29. Kim, M. A., S. Do Yoon, J. S. Lee, and C.-M. Lee, "Melanin-peg nanoparticles as a photothermal agent for tumor therapy," *Materials Today Communications*, Vol. 25, p. 101575, 2020.

30. Li, Y., X. Liu, W. Pan, N. Li, et al., "Photothermal therapy-induced immunogenic cell death based on natural melanin nanoparticles against breast cancer," *Chemical Communications*, Vol. 56, no. 9, pp. 1389–1392, 2020.

31. Liu, D., H. Huang, B. Zhao, and W. Guo, "Natural melanin-based nanoparticles with combined chemo/photothermal/photodynamic effect induce immunogenic cell death (icd) on tumor," *Frontiers in Bioengineering and Biotechnology*, Vol. 9, p. 635858, 2021.

32. Moser, E., A. Stadlbauer, C. Windischberger, H. H. Quick, et al., "Magnetic resonance imaging methodology," *European Journal of Nuclear Medicine and Molecular Imaging*, Vol. 36, pp. 30–41, 2009.

33. Barkhausen, J., T. Kahn, G. A. Krombach, C. K. Kuhl, et al., "White paper: interventional mri: current status and potential for development considering economic perspectives, part 2: liver and other applications in oncology," in *RöFo-Fortschritte auf dem Gebiet der Röntgenstrahlen und der bildgebenden Verfahren*, Vol. 189, pp. 1047–1054, © Georg Thieme Verlag KG, 2017.

34. Fraum, T. J., D. R. Ludwig, M. R. Bashir, and K. J. Fowler, "Gadolinium-based contrast agents: a comprehensive risk assessment," *Journal of Magnetic Resonance Imaging*, Vol. 46, no. 2, pp. 338–353, 2017.

35. Chen, A., J. Sun, S. Liu, L. Li, et al., "The effect of metal ions on endogenous melanin nanoparticles used as magnetic resonance imaging contrast agents," *Biomaterials Science*, Vol. 8, no. 1, pp. 379–390, 2020.

36. Baysoy, E., G. Kaleli-Can, A. Özcan, C. Liu, et al., "Passive device tracking for interventional mri with ferric ion chelated natural melanin nanoparticles," in *Proceedings of the International Society for Magnetic Resonance in Medicine (ISMRM) 2023*, Vol. 31, p. 4384, 2023.

37. Baysoy, E., G. Kaleli-Can, B. Ayan, Ö. Kocatürk, et al., "Enhanced balloon catheter visualization with biocompatible melanin nanoparticles in 3t mri," *Journal of Cardiovascular Magnetic Resonance*, Vol. 26, 2024.

38. Seçkin, İ., B. Kaleli, E. Sönmez, G. K. Can, et al., "Coating of nitinol guidewire with manganese ion chelated natural melanin nanoparticles for mri," in *2024 Medical Technologies Congress (TIPTEKNO)*, pp. 1–4, IEEE, 2024.

39. Miao, Z.-H., H. Wang, H. Yang, Z.-L. Li, et al., "Intrinsically mn2+-chelated polydopamine nanoparticles for simultaneous magnetic resonance imaging and photothermal ablation of cancer cells," *ACS Applied Materials & Interfaces*, Vol. 7, no. 31, pp. 16946–16952, 2015.

40. Kang, S., R. Baskaran, B. Ozlu, E. Davaa, et al., "[t. sub. 1]-positive [mn. sup. 2+]-doped multi-stimuli responsive poly (l-dopa) nanoparticles for photothermal and photodynamic combination cancer therapy.," *Biomedicines*, Vol. 8, no. 10, pp. NA–NA, 2020.

41. Dong, Z., H. Gong, M. Gao, W. Zhu, et al., "Polydopamine nanoparticles as a versatile molecular loading platform to enable imaging-guided cancer combination therapy," *Theranostics*, Vol. 6, no. 7, p. 1031, 2016.

42. Jakubiak, P., C. Cantrill, A. Urtti, and R. Alvarez-Sánchez, "Establishment of an in vitro–in vivo correlation for melanin binding and the extension of the ocular half-life of small-molecule drugs," *Molecular Pharmaceutics*, Vol. 16, no. 12, pp. 4890–4901, 2019.

43. Cuzzubbo, S., and A. F. Carpentier, "Applications of melanin and melanin-like nanoparticles in cancer therapy: A review of recent advances," *Cancers*, Vol. 13, no. 6, p. 1463, 2021.

44. Butler, S. L., and Z. Zhang, "Forward modeling of geophysical electromagnetic methods using comsol," *Computers & Geosciences*, Vol. 87, pp. 1–10, 2016.

45. Repenko, T., A. Rix, A. Nedilko, J. Rose, et al., "Strong photoacoustic signal enhancement by coating gold nanoparticles with melanin for biomedical imaging," *Advanced Functional Materials*, Vol. 28, no. 7, p. 1705607, 2018.

46. Dubnishchev, Y. N., V. A. Arbuzov, E. V. Arbuzov, V. S. Berdnikov, et al., "Study of convective structures and phase transition induced in a water layer by non-stationary boundary conditions," *Journal of Physics: Conference Series*, Vol. 1421, no. 1, p. 012047, 2019.

47. Giering, K., O. Minet, I. Lamprecht, and Müller, G., "Review of thermal properties of biological tissues," *Laser-Induced Interstitial Thermotherapy*, pp. 45–65. Bellingham, WA: SPIE Opt. Eng. Press, 1995.

48. Khurgin, J. B., and G. Sun, "Enhancement of optical properties of nanoscaled objects by metal nanoparticles," *Journal of the Optical Society of America B*, Vol. 26, no. 12, pp. B83–B95, 2009.

49. Gille, W., "Particle and Particle Systems Characterization: Small-Angle Scattering (SAS) Applications," CRC Press, 2013.

50. Wang, R., C. Xu, and J. Sun, "ACS applied materials & interfaces," *ACS Applied Materials & Interfaces*, Vol. 6, no. 2, pp. 1044–1052, 2014.